وزارة التعليم العالي والبحث العلمي
Ministry of Higher Education and Scientific Research

University of Saâd Dahleb Blida 1
Institute of Aeronautics and Space Studies
Department of Aeronautical Construction

Manuscript

Towards the obtainment of the Master's degree in Aeronautics
Specialty: **Aircraft Propulsion**

Numerical Investigation of the Effect on Aerodynamic Performances of the Inter-Propeller Distance in a Contra-Rotating Propeller

Under the supervision of:

- Dr. BENTRAD Hocine
- Dr. BEKHTI Ahmed
- Mr. LAAZAB Sbâa

Submitted by:

- Mr. MOULAI Hamza

Jury Members:

- Dr. ABDALLAH EL HIRTSI Ahmed — President
- Dr. CHEGRANI Ahmed — Examiner

Defended on June 29th, 2024

ABSTRACT

The present thesis focuses on the numerical investigation of low-Reynolds contra-rotating propellers (CRPs) aerodynamics relevant in unmanned air vehicle applications. The objective of this study is to assess the effect of inter-propeller distance on the aerodynamic performances of the system (indicated by the thrust coefficient C_T, the power coefficient C_P and the efficiency η).

Two numerical approaches are considered: the vortex lattice method (VLM) through the OpenVSP software, and computational fluid dynamics (CFD) with OpenFOAM and ANSYS-Fluent using the standard k-ε turbulence model. Simulations are performed on an isolated propeller for multiple advance ratios and compared to the experimental data available of the propeller with the closest geometry in order to assess the two proposed approaches. Then, simulations for CRP configurations are executed (all advance ratios as in the isolated case are considered in VLM, whereas simulations have been executed for the maximal efficiency case using CFD) and compared with each other.

Different results have been obtained using the two approaches. However, the conclusion that CRP systems are advantageous for the maximal efficiency advance ratio is common. Results indicate that spacing has little to no effect on efficiency; but CFD predicts an increase of thrust with the increase of spacing meaning that a higher inter-propeller distance allows for higher thrust value while conserving efficiency.

Keywords: Contra-rotating propeller; OpenFOAM; OpenVSP; ANSYS-Fluent; inter-propeller distance; CFD

RÉSUMÉ

Le présent mémoire se concentre sur l'étude numérique de l'aérodynamique des hélices contrarotatives (CRP) dont les applications s'étendent dans le domaine des drones. L'objectif de cette étude est d'évaluer l'effet de l'espacement (distance inter-hélice) sur les performances aérodynamiques du système (indiquées par le coefficient de poussée C_T, le coefficient de puissanceC_P et le rendement η).

Deux approches numériques sont considérées : la méthode « vortex lattice » (VLM) avec le logiciel « OpenVSP », et la dynamique des fluides numérique (CFD) avec OpenFOAM et ANSYS-Fluent comme logiciels en employant le modèle de turbulence k-ε. Les simulations sont exécutées sur une hélice isolée pour plusieurs coefficients d'avancement et sont comparées aux données expérimentales de l'hélice à la géométrie la plus proche afin d'évaluer les deux approches. Puis, des simulations sur les cas contrarotatifs sont exécutées (tous les coefficients d'avancement sont considérées avec la VLM, mais seulement le case de rendement maximal pour la CFD) et sont comparées entre-elles.

Différents résultats sont obtenus à l'aide des deux approches. Cependant, la conclusion que les CRP sont plus avantageuses pour le coefficient d'avancement donnant un rendement maximal est commune. Les résultats obtenus indiquent que l'espacement a un effet négligeable sur le rendement, mais la CFD prédit une augmentation de la poussée avec l'augmentation de l'espacement, ce qui veut dire qu'il est possible d'obtenir des valeurs supérieurs de la poussée en conservant le même rendement.

Mots clé : Hélices contrarotatives ; OpenFOAM ; OpenVSP ; ANSYS-Fluent ; distance inter-hélice ; CFD

ملخص

تركز هذه المذكرة على الدراسة الرقمية لديناميكية الهواء للمروحيات ذات الدوران المعاكس وذات رقم رينولدز المنخفض، ذات تطبيقات في مجال الطائرات بدون طيار. الهدف من هذه الدراسة هو تقييم تأثير المسافة بين المروحتين على الأداء الديناميكي للنظام (المشار إليه بمعامل الدفع C_T ، معامل الإستطاعة C_P ، والكفاء η)

يتم النظر في نهجين رقميين: طريقة Vortex Lattice (VLM) من خلال برنامجOpenVSP ، و ديناميك الموائع الحاسبية (CFD) باستخدام OpenFOAM و ANSYS-Fluent من خلال نموذج k-ε القياسي. يتم إجراء المحاكاة على مروحة معزولة لمعاملات تقدم متعددة ومقارنتها بالبيانات التجريبية المتاحة للمروحة ذات الشكل الأقرب من أجل تقييم النهجين المقترحين. ثم يتم تنفيذ محاكاة لأنظمة CRP) جميع معاملات التقدم تعتبر فيVLM ، بينما تم تنفيذ المحاكاة للحالة التي تحقق أقصى كفاءة باستخدام (CFD ومقارنتها مع بعضها البعض.

تم الحصول على نتائج مختلفة باستخدام النهجين. ومع ذلك، الاستنتاج بأن أنظمة CRP هي الأحسن لنسبة التقدم الكفاءة القصوى مشترك. تشير النتائج إلى أن المسافة بين المرويتين لها تأثير ضئيل على الكفاءة؛ ولكن CFD يتنبأ بزيادة الدفع مع زيادة المسافة، مما يعني أن مسافة أكبر بين المروحتين تسمح بقيمة دفع أعلى مع الحفاظ على الكفاءة.

الكلمات المفتاحية: مروحة الدوران المعاكس؛OpenFOAM ؛OpenVSP ؛ANSYS-Fluent ؛ مسافة بين المروحتين؛CFD

I dedicate this work to:

My mother, your unwavering love, support and sacrifices, you spared neither efforts nor expenses into making me the man I am today;

My father, who always believed in me and encouraged me, you taught me the values of resilience, perseverance and pursuit of excellence;

My brother, your friendship, camaraderie and belief in me have been a constant source of support and motivation;

For the blood, sweat and tears you all shed these years, a testimony of your unconditional, relentless and steadfast support.

ACKNOWLEDGMENTS

First and foremost, I thank God for giving me the patience, perseverance and fortitude throughout my study years culminating with the competition of this modest work.

I would like to express my profound acknowledgments towards:

My esteemed supervisors Dr. Bentrad Hocine, Dr. Bekhti Ahmed and Mr. Lazab Sbâa for their continuous support, wisdom and rigour throughout this academic endeavour, their teachings, advice and suggestions have been an indispensible help;

The aerodynamics research team at the Wind Energy Division of the Renewable Energies Development Centre, for giving me the opportunity to use their computational capabilities throughout a comprehensive research internship;

The researchers, teachers and staff at the Laboratory of Aeronautical Science of the University of Saâd Dahleb Blida 1, for giving me the opportunity to fully exploit their computational resources, their trust in my work and their steadfast support;

The examination board jury members, for evaluating the presented work, their insights and commentaries are most welcomed;

My family and friends, for all their continuous support, as well as everyone who contributed either directly or indirectly to the completion of this project.

TABLE OF CONTENTS

LIST OF FIGURES

LIST OF TABLES

NOMENCLATURE

Latin alphabet:

A: Area of the disc swept by the propeller's blades
A_{aft} : Area of afterward propeller
A_{fwd}: Area of forward propeller
b: Number of blades
c: Chord
c_{ref}: Reference chord
C_D: Drag coefficient
C_P: Power coefficient
C_Q: Torque coefficient
C_T: Thrust coefficient
C_μ: Coefficient in k-ε model
C_1: Coefficient in k-ε model
C_2: Coefficient in k-ε model
d: Inter-propeller distance
D: Diameter
D_{aft}: Diameter of afterward propeller
D_{fwd}: Diameter of forward propeller
E: Wall roughness constant
f_x: Volume force in the x direction
f_y: Volume force in the y direction
f_z: Volume force in the z direction
i: Spatial index
j: Spatial index
J: Advance ratio
k: Turbulent kinetic energy
m: Counting index
M: Number of panels
n: Counting index
N : Rotational speed (in revolutions per second)
N_{aft} : Rotational speed of afterward propeller (in revolutions per second)
N_{fwd} : Rotational speed of forward propeller (in revolutions per second)
p: Pressure
P: Power
P_{aft}: Power of afterward propeller
P_{fwd}: Power of forward propeller
P_i: Induced power
P_u: Useful power
Q: Torque
Q_{aft}: Torque of afterward propeller
Q_{fwd}: Torque of forward propeller
r: Radius
R: Total radius of the propeller
R_{hub}: Radius at the propeller's hub
R_{ij}: Reynolds stress tensor
t: Time variable
T: Thrust
T_{aft}: Thrust of afterward propeller
T_{fwd}: Thrust of forward propeller
u: Velocity in the x direction
$u^*_{a(n)}$: Total induced axial velocity
$\bar{u}^*_{a(n,m)}$: Axial influence function
$u^*_{t(n)}$: Tangential axial velocity
$\bar{u}^*_{t(n,m)}$: Tangential influence function
v: Velocity in the y direction
V: Velocity
$V_{a(m)}$: Axial velocity
$V_{t(m)}$: Tangential velocity
V^*: Total relative velocity
v_i: Induced velocity
w: Velocity in the z direction
x: Spatial variable
y: Spatial variable
y_P : Distance between the nearest computational node to the wall
z: Spatial variable

Greek alphabet:

β_i: Aerodynamic pitch angle
δ_{ij}: Kroenicer symbol
Γ: Circulation strength
ε: Turbulent dissipation energy

μ: Dynamic viscosity
μ_T: Turbulent viscosity
η: Efficiency
η_i: Ideal efficiency
κ: Von Karman constant
ρ: Density
σ_k: Coefficient in k-ε model
σ_ε: Coefficient in k-ε model
τ: Shear stress
φ: Oscillations frequency

Abbreviations:

AFT: Afterwards
BEMT: Blade element momentum theory
CFD: Computational fluid dynamics
CRP: Contra-rotating propeller
Exp: Experimental
FOAM: Fields operation and manipulation
FOM: Figure of merit
FVM: Finite volume method
FWD: Forward
GUI: Graphical user interface
GPL: General public license
MRF: Multiple reference frame
NASA: National aeronautics and space administration
RANS: Reynolds averaged Navier-Stokes
RNG: Re-normalization group
RPM: Revolutions per minute
RSM: Reynolds stress modelling
SST: Shear stress transport
UAV: Unmanned air vehicle
VSP: Vehicle sketch pad

INTRODUCTION

Whether for economic or environment sustainability purposes, the quest for efficient and reliable propulsion systems is one of utmost importance for industries and researchers alike. As aircraft design evolves to meet the demands of increased efficiency and reduced emissions for low-speed aircraft, propulsion configurations using propellers are privileged, such as contra-rotating propellers (CRPs) but also ducted and slated propellers, end even bio-mimetic solutions. The scope of the following study, however, concerns contra-rotating propellers applied to unmanned air vehicles (UAV) in the incompressible regime; indeed low-Reynolds propellers which were traditionally used in aircraft modelling have found more application with the development of UAV technology.

CRPs consist of two coaxially aligned propellers rotating in opposite directions; they offer an advantage in terms of thrust augmentation and negate the reaction torque, thus presenting a compelling option for next-generation UAVs, in fact such a configuration was used on the Insight UAV which mission is to scout Martian terrain from an aerial perspective.

However, the aerodynamic characteristics of CRPs still present challenges that require thorough investigation. Traditional experimental as well as engineering methods such as the vortex lattice method provide valuable insights and allow engineers to take design decisions, but since experimental methods are limited by cost and installations and engineering ones don’t allow the assessment of the complex flow patterns; thus, in order to truly understand the interaction between the propellers in CRP configurations, Computational Fluid Dynamics (CFD) presents itself as a powerful tool that enables the prediction of performance as well as to fully take into account the interaction between the propellers, while maintaining a low cost compared to experimental methods and offering results in the whole computational domain.

The present study endeavours to contribute to the advancement of a more sustainable and economic UAV propulsion technology through a comprehensive study of contra-rotating propellers is two parts: using the vortex lattice method (VLM) and CFD to assess the effect of inter-propeller distance. The objective of this work is to asses the influence of the axial spacing between the two propellers on the system’s efficiency.

The present thesis is structured as follows: firstly, an overview on propellers and the relevant performance coefficients is given; secondly, a literature review on the research conducted on propellers (and CRPs in particular); then a first approach is presented using the vortex lattice method (VLM); next the second CFD approach is laid out, where the mathematical modelling and the numerical framework are given, followed by the results. And finally, general conclusions and recommendations are drawn from the obtained results.

CHAPTER 1:
OVERVIEW ON PROPELLERS

CHAPTER 1: OVERVIEW ON PROPELLERS

A propeller can be defined as "a device for proving a force of thrust, at the expense of power generated by a motor, for driving a craft of some sorts through a fluid medium, such as air or water". Devices such as paddle wheels and various feathering blade contraptions correspond to this definition, but the "air screw propeller has been universally adopted for aircraft propulsion" because, as its name implies, "it screws or twists its way through the air" [26]; thus all after mentioned propellers will be of the air screw type.

Albeit being the first mean of aeronautical propulsion, propellers have stood the test of time and are still used in a multitude of aircraft (and more recently UAVs in particular) because in the subsonic regime propeller engines have a lower fuel consumption than jet engines (equivalent to a higher efficiency).

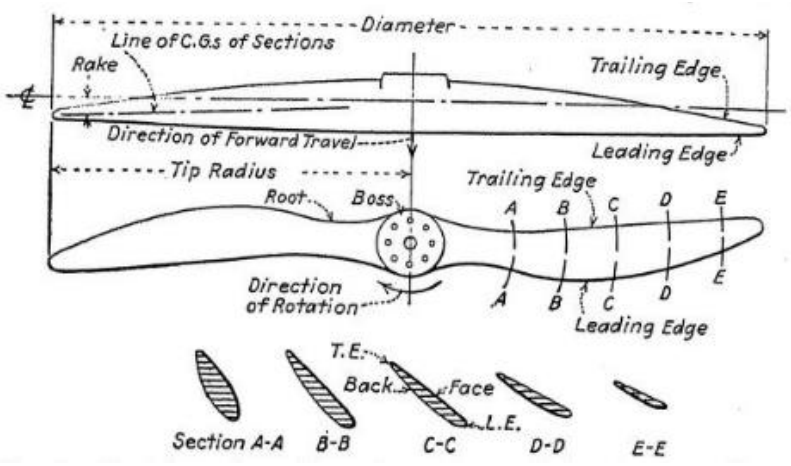

Figure 1-1: Nomenclature of a propeller [26]

The nomenclature of a propeller is given in Figure 1-1; propellers consist of blades connected to a central boss. The diameter of the propeller is the diameter of the disc swept by the blades. The pitch is the advance per revolution: if the propeller is in operating conditions, the pitch would be an effective pitch; in addition there are two other kinds of pitch which are the geometric pitch (the advance of the propeller if it were moving along a helix having an angle equal to the blade angle), and the experimental pitch (which corresponds to the advance per revolution with no thrust production) [26].

A propeller can be mounted at the front of the body (fuselage, wing), or at the rear; in the former case it is called a tractor propeller, and in the latter it is called a pusher propeller [26].

Each blade of the propeller can be defined as a rotating wing, however for a performance study, non-dimensional variables are used. Dimensional analysis considering the diameter D, rotational speed N (or propeller frequency in revolutions per second), air density ρ, free-stream velocity V, thrust T, torque Q and power P has been performed by reference [19] yielding the advance ration J, the thrust coefficient C_T, the torque coefficient C_Q, the power coefficient C_P, and the efficiency η:

$$J = \frac{V}{ND} \tag{2.1}$$

$$C_T = \frac{T}{\rho N^2 D^4} \tag{2.2}$$

$$C_Q = \frac{Q}{\rho N^2 D^5} \tag{2.3}$$

$$C_P = \frac{P}{\rho N^3 D^5} \tag{2.4}$$

$$\eta = \frac{C_T J}{C_P} \tag{2.5}$$

In the case of CRPs, the thrust, torque and power coefficients, the formulation from reference [21] is used:

$$C_T = \frac{T_{fwd} + T_{aft}}{\rho 0.25\left(N_{fwd}^2 + N_{aft}^2\right)\left(D_{fwd}^4 + D_{aft}^4\right)} \tag{2.6}$$

$$C_Q = \frac{Q_{fwd} + Q_{aft}}{\rho 0.25\left(N_{fwd}^2 + N_{aft}^2\right)\left(D_{fwd}^5 + D_{aft}^5\right)} \tag{2.7}$$

$$C_P = \frac{P_{fwd} + P_{aft}}{\rho 0.25\left(N_{fwd}^3 + N_{aft}^3\right)\left(D_{fwd}^5 + D_{aft}^5\right)} \tag{2.8}$$

CHAPTER 2:
LITERATURE REVIEW

CHAPTER 2: LITERATURE REVIEW

Propellers were extensively studied since the beginning of aeronautics as shown by Weick in his book [26], in which he summarizes and builds on the works of the previous decade: actuator disk theory, blade momentum theory and even an introduction to vortex theory are described. As for contra-rotating propellers, McCoy [13] dates the first discussion of the benefits of such a system compared to single propellers to Lanchester in 1907. However, the first helicopter patent (which had contra-rotating rotors) was given to Henry Bright in 1859 by the British Patent Office [6].

Since then, many advancements in propeller knowledge were made, especially with numerical methods related to potential flows (panel and vortex lattice methods), and more recently with computational fluid dynamics. As CFD is a relatively new method to assess CRPs performance, most research in the last century was either experimental, or with panel or vortex methods as shown by Coleman is his survey [6].

Actual research on propellers in general and CRPs in particular is still conducted (as shown by the after mentioned publications) and can be split into three axes: non-CFD numerical methods, CFD and experiments, however most work on propellers was done for marine applications.

In 2010, Grassi et al. [9] compared the latest numerical methods at the time, one using lifting line theory for the design and another using lifting surface theory for the performance, in the case of a CRP (4 blades for the front and 3 for the aft propeller) setup with experimental results from cavitation tunnel tests. The CRP was to be installed in a commercial pod drive system, a marine application. They obtained a satisfying agreement between numerical and experimental results (although only experimental tendencies are given in their article for industrial reasons) around the design point. They concluded that the used numerical methods are sufficient for a design phase in the case of marine applications.

In 2011, Brandt and Selig [4] conducted an experimental study of 79 propellers (almost all of them in the 9 to 11 inches in diameter range, dual bladed). They focused solely on the low-Reynolds number range with UAV applications in mind. They found that the effect of low-Reynolds conditions is significant, and degrades the performance of the propeller. Indeed, they reported efficiencies ranging from 0.28 (for an exceptionally poor propeller) to a peak near 0.65.

In 2016, Stajuda et al. [20] published a CFD study giving guidelines for single propellers simulations using the Multiple Reference Frame approach, with a dual bladed propeller case as an example; results were compared with experiments. They used the commercial software ANSYS-CFX and the RANS (Reynolds Averaged Navier Stokes) SST k-ω (Shear Stress Transport) model to compute their results. The main advantage of this approach is the ability to conduct steady flow simulations; however the authors study showed that results are very sensitive to the rotating domain thickness, hence experimental results are always needed for validation.

In 2017, Feng et al. [8] conducted a CFD study using the SST k-ω turbulence model to evaluate the hydrodynamic performance of a 4 blades marine CRP with the Star CCM+ software; they used the MRF approach and a fully structured grid. They compared numerical results with experiments and results showed a fair agreement.

Triet et al. [25], in 2018, conducted a CFD study for a 3 bladed marine single propeller using the k-ε turbulence model and the MRF approach with the OpenFOAM software. Unstructured tetrahedral mesh was used, and y+ values was as low as 10; results showed good agreements with experiments for low advance ratios (under 0.7).

In their paper, in 2019, Su et al. [22] explored single, tandem and contra-rotating propeller configurations for marine applications for different advance coefficient. They used standard k-ε, k-ε RNG, SST k-ω and RSM (Reynolds stress modelling) turbulence models to assess the performance. Comparison with experiments showed that the RSM model is the most accurate, whereas the standard k-ε error is the largest. The efficiency of the CRP configuration was found to be the highest of the three.

In that same year, Thiele et al. [24] proposed a BEMT (Blade Element Momentum Theory) method to evaluate the performances of single and counter-rotating UAV propellers. The model showed promising results in various flow configurations, however it is still limited since it does not compute trailing vortices and wake effects; the interaction between the two propellers has been modelled only using induced velocities. However, as the model is not computationally demanding, it can be used in an optimization strategy during the design phase.

In 2020, Panjwani et al. [15] developed a coupled CFD-BEMT using OpenFOAM and QBlade and applied it to a CRP. They also presented an experimental approach to predict

performances of single and contra-rotating propellers; however their approach presents their results in function of the rotational speed and not the advance ratio. The results of the coupled CFD-BEMT method were in good agreement with the experiments, which makes this approach interesting for an optimization in the design phase.

In 2023, Wenhui and Kun [27] investigated the effects of axial spacing in a 6 blades CRP using the unsteady RANS SST k-ω turbulence model and sliding mesh technique. The study showcased the importance of spacing in CRP design. Indeed, the authors found that from the four studies cases, the one with a spacing of 0.25D gives a higher overall efficiency. However, only one advance ratio of J=2.5 was considered.

In that same year, Lopez and Juando [12] conducted a CFD study using OpenFOAM on various CRP configurations (for applications in hydrofoil vessels) varying the number of blades and the diameters of the propellers. Blade imbalance is found to be helpful as it minimizes the likelihood of resonance, a smaller diameter for the aft propeller is also recommended in order to exploit the induced velocity effect while avoiding the trailing tip vortices. The authors also suggest minimizing the spacing between the propellers.

Also in 2023, Russo et al. [17] conducted a thrust and noise experimental assessment of a CRP for UAV applications. Their experimental setup did not allow a study considering various advance coefficients, so rotational velocity was considered instead to differentiate between cases. They found that overall thrust does not significantly vary with the spacing between propellers; however the thrust of individual propellers is significantly affected with the single propeller outperforming the individual ones in the CRP configurations. Concerning noise measurements, they found that there is a high variability at the low RPM range, however at a high RPM spacing does not affect noise generation.

Aside from the aforementioned articles, several Master's and PhD theses have been written in this field. For example concerning Master's theses, Kravitz and Chryssostomidis [10], contribute to the already existing open source software "OpenProp" for marine applications (which works using lifting line theory) by adding off-design analysis for CRPs. Sercan & Aksel [18], used OpenProp to design a marine CRP, and then used CFD to conduct performance analysis. And concerning PhD theses, Štorch [21] coupled a 2D boundary layer to a 3D panel model for propeller studies; the model was found to be more accurate than lifting line theory, especially in the case of CRPs; whereas Bouregba [3] conducted a CFD study using RANS SST k-ω turbulence model and sliding mesh technique for a marine CRP;

the effects of axial spacing, angular displacement and twist were investigated, adopting a moderate negative twist angle was found to be effective, however the research wasn't backed with experimental data.

The aforementioned publications and theses showcase that CRP aerodynamics is a very active research field. The range and complexity of the possible cases makes drawing general conclusions hard, as performances are very sensitive to conditions change, making further research worthwhile.

CHAPTER 3:
SIMULATIONS USING THE VORTEX LATTICE METHOD

CHAPTER 3: SIMULATIONS USING THE VORTEX LATTICE METHOD

3.1. VORTEX LATTICE METHOD THEORY

The vortex lattice method is a "thin surface" method that is used mainly in engineering applications at the first stages of design. A potential incompressible flow is assumed (inviscous compressible flow).

In this model, a lifting line distribution is supposed for each blade, it is then divided into M panels of length dr.The induced velocities by the propeller are calculated at control points located at the middle of each panel. The continuous bound circulation distribution is replaced with a discrete distribution lengthwise with strength $\Gamma_{(m)}$ located at radius$r_{(m)}$. The helical free vortex sheet characteristic of the lifting line method is replaced with concentrated helix vortices shed from each panel boundary. Therefore, the discrete circulation distribution can be thought as a set of vortex horseshoes, each an assembly of one bound vortex segment with two free trailing helix vortices. The strength of each free trailing vortex is equal to the strength difference of two adjacent bound vortices along the blade. The total induced velocity at each computational point is the summation of the velocity induced from an individual horseshoe vortex at that point [10]:

$$u^*_{a(n)} = \sum_{m=1}^{M} \Gamma_{(m)} \bar{u}^*_{a(n,m)} \tag{4.1}$$

$$u^*_{t(n)} = \sum_{m=1}^{M} \Gamma_{(m)} \bar{u}^*_{t(n,m)} \tag{4.2}$$

Where:

- $u^*_{a(n)}$: total induced axial velocity;
- $u^*_{t(n)}$: total induced tangential velocity;
- $\Gamma_{(m)}$: circulation strength at radius $r_{(m)}$;
- $\bar{u}^*_{a(n,m)}$: axial influence function;
- $\bar{u}^*_{t(n,m)}$: tangential influence function.

Integrating equations (4.1) and (4.2) under discrete form yields:

$$T = \rho b \sum_{m=1}^{M} \left\{ \left[V_{t(m)} + v_i r_{(m)} + u^*_{t(m)} \right] \Gamma_{(m)} \Delta r - \frac{1}{2} V^*_{(m)} \left[V_{a(m)} + u^*_{a(m)} \right] c_{(m)} C_{D(m)} \Delta r \right\} \quad (4.3)$$

$$Q = \rho b \sum_{m=1}^{M} \left\{ \left[V_{a(m)} + v_i r_{(m)} + u^*_{a(m)} \right] \Gamma_{(m)} \Delta r - \frac{1}{2} V^*_{(m)} \left[V_{t(m)} + u^*_{t(m)} \right] c_{(m)} C_{D(m)} \Delta r \right\} \quad (4.4)$$

Where:

- $V_{a(m)}$: axial velocity at point m;
- $V_{t(m)}$: tangential velocity at point m;
- $V^*_{(m)}$: total induced velocity at point m;
- v_i: induced velocity;
- $c_{(m)}$: chord length at point m;
- $C_{D(m)}$: drag coefficient of the airfoil at point m.

3.2. FRAMEWORK OF STUDY WITH OPENVSP

OpenVSP (Open Vehicle Sketch Pad) was developed by NASA in the 1990s' and released as open-source in 2012 (which can be downloaded at https://openvsp.org/. It is a parametric aircraft geometry tool and supports many engineering analyses, including aerodynamic analyses using the vortex lattice method [14]. VSPAero, which is the component of OpenVSP responsible for aerodynamic analyses, offers the possibility to study propellers represented as actuator disks or rotating blades using the vortex lattice method (with an extensive guide being available online at https://vspu.larc.nasa.gov/).

3.2.1. USED MACHINE

In order to give context to this study, it is important to indicate the machine used for the simulations with OpenVSP. The properties of the machine being the following:

- Processor: Intel® Core™ i5 CPU M 560 @ 2.67 GHz, 2 cores, 4 threads;
- RAM: 6.00 GB DDr3, 1200 MHz.

.

3.2.2. GEOMETRY GENERATION

The geometry considered for our test cases is taken from the open access library of grabcad.com (the link to download the geometry being the following: https://grabcad.com/library/low-reynolds-propeller-for-ultra-light-aircrafts-1). The geometry is in multiple formats and the airfoil data file is given (the propeller is 15''*8'' with an Eppler E853 airfoil); however, the hub of the propeller is neglected for meshing considerations in the CFD part, in order to assess the same geometry.

Importing the geometry directly to OpenVSP does not work as it does not recognize it as a propeller (rather as a fuselage/pod) and cannot distinguish between the leading edge and trailing edge. Hence, the propeller had to be generated using the internal design tool. As the SolidWorks part format is given, it is possible to obtain the necessary parameters (chord, sweep, twist) at multiple stations and insert them into the design tool to obtain the same propeller.

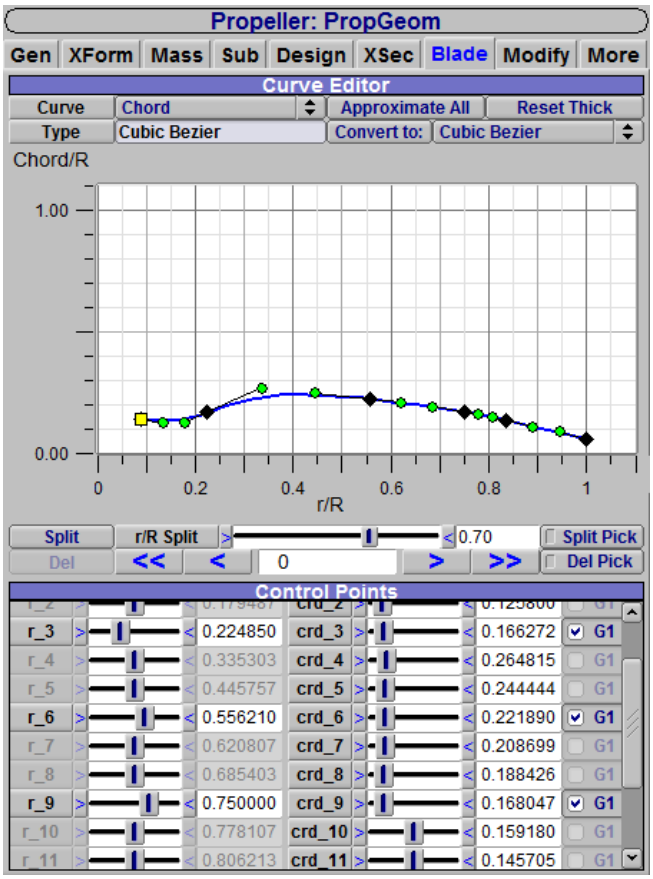

Figure 3-1: "Blade" tab of the OpenVSP design tool for propellers

Figure 3-1 and Figure 3-2 show the most relevant tabs of the graphical user interface (GUIs) of the design tool. It is to be noted that throughout the entirety of the present work, the international units system is used.

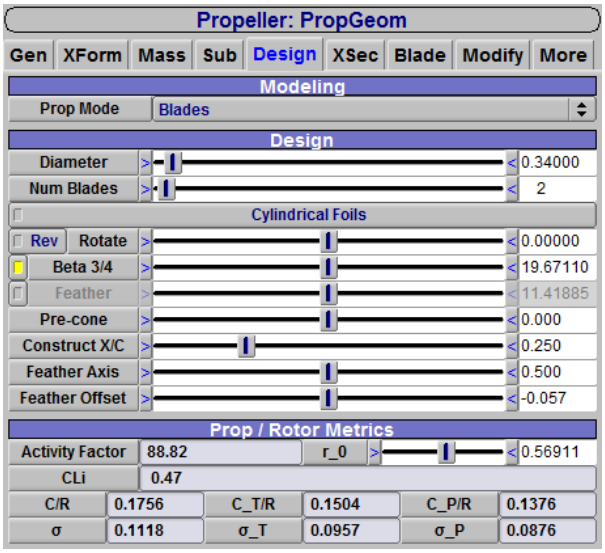

Figure 3-2: "Design" tab of the design tool for propellers in OpenVSP

3.2.3. COMPUTATIONAL GRID

The computational grid is generated at the same time as the geometry in the integrated propeller design module of OpenVSP. The default grid is a uniform grid with rectangular panels; the minimal number of panels acceptable by the software is 25*17 panels. Computations using a finer grid of 35*25 panels have also been done in the isolated propeller case to assess grid sensitivity.

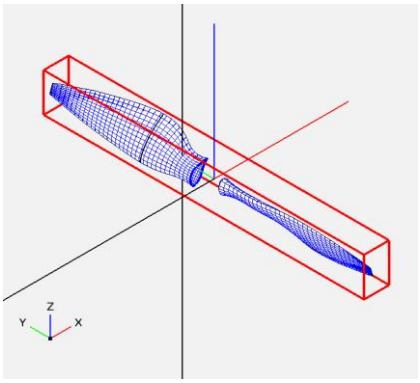

Figure 3-3: Geometry and computational grid of the propeller

The obtained geometry, as well as the computational grid, are shown on Figure 3-3, it is important to note that the black axes are offset for visual purposes; the axes used in computations are the coloured ones (red, green and blue).

For the CRP geometry, the same propeller is used for both rotors, as shown in Figure 3-4.

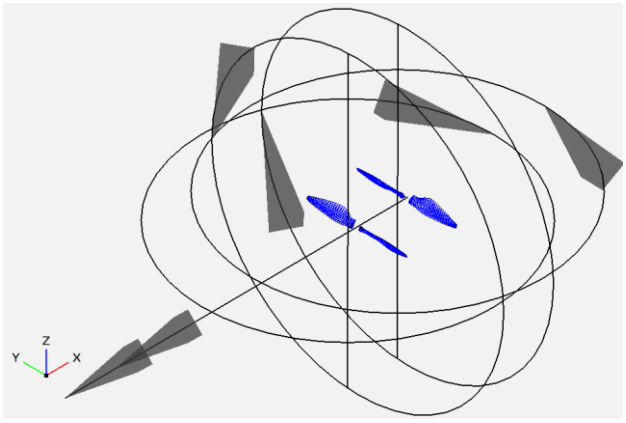

Figure 3-4: Geometry and computational grid of CRP configuration with inter-rotor distance of 0.5D

3.2.4. SIMULATION CASES

Simulations have been performed for various advance ratios ranging from 0.231 to 0.924 to capture the efficiency maximum. A single isolated propeller (for reference) and CRPs with dimensionless inter-propeller distances "d" of d=0.3D, d=0.5D and d=1D are chosen. The same rotational speed on both propellers is imposed, additional cases at d=0.08D and d=0.1D are also performed for some of the advance ratios.

Reference values used for calculations are the area of the equivalent propulsive disc, the diameter of the propeller, and the three-quarters chord (c at 0.75R).

3.2.5. VSPAERO SET-UP

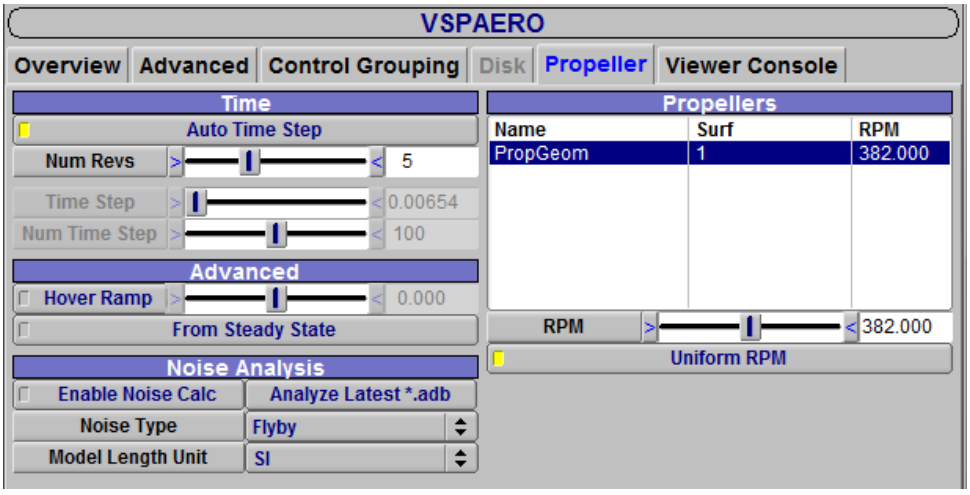

Figure 3-5: "Propeller" tab of the VSPAero GUI

Aerodynamic simulations are performed using the VSPAero module of OpenVSP. The GUI of the software module is shown in Figure 3-6 and Figure 3-5 with all the relevant boundary conditions for the J=0.462 case; rotational speed of the propeller(s) is changed accordingly to adjust for other advance ratios cases while free stream velocity is kept equal to 1 m/s.

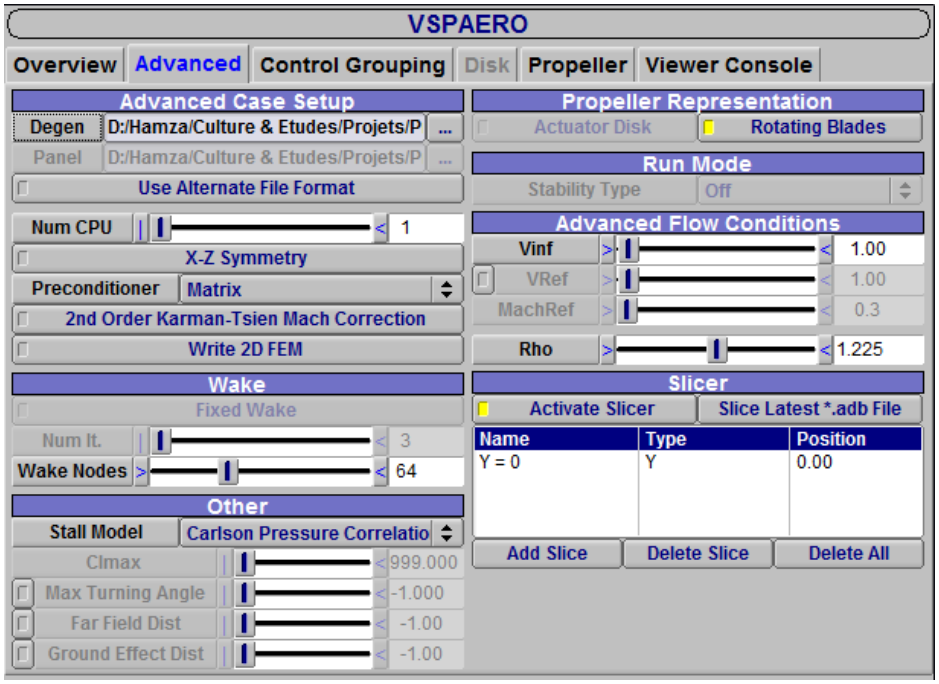

Figure 3-6: "Advanced" tab of the VSPAero GUI

3.2.6. Grid Sensitivity Analysis

Grid sensitivity is assessed using two grids: a coarse 25*17 panels grid and a fine 35*25 panels for multiple advance coefficients.

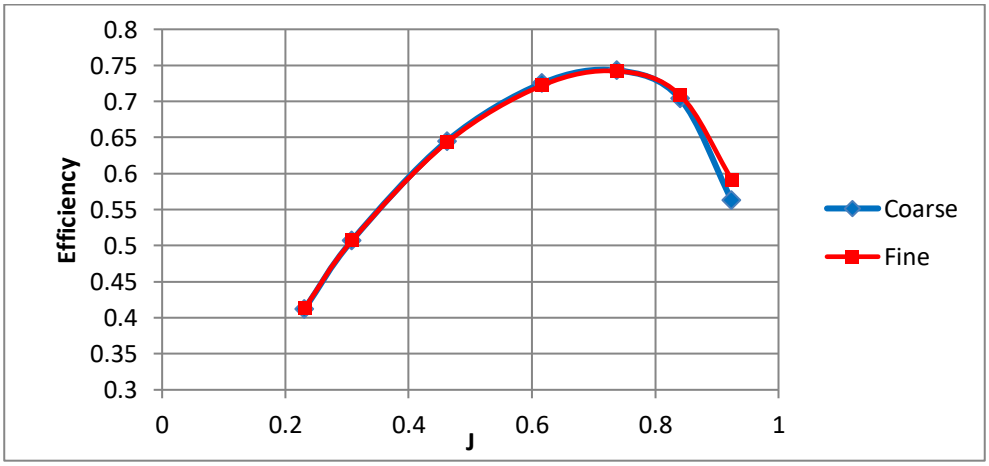

Figure 3-7: Propulsive efficiency plot as a function of the advance ratio

Grid independence is assessed by using the propulsive efficiency as the monitoring parameter. It can be seen on Figure 3-7 that the difference between the results for the fine and coarse grid is minimal; hence all further calculations are done on the coarse grid to reduce the computing time. A coarser grid could not be generated on OpenVSP for propeller mode.

3.3. RESULTS

3.3.1. ISOLATED PROPELLER

Simulations have been performed on three sets of cases, two cases where the RPM is fixed (at 3,000 RPM and 6,000 RPM) and a case where the upstream velocity is fixed.

The results corresponding to the 3,000 RPM regime are compared to the experimental data of the Graupner CAM Slim 10x8 [4] as they have the same reference twist angle (around 20°) and have a similar overall geometry (since the airfoil used, the feather and the construction line were not given, this specific propeller couldn't be modelled). Although the propellers are not identical, performances are expected to be close.

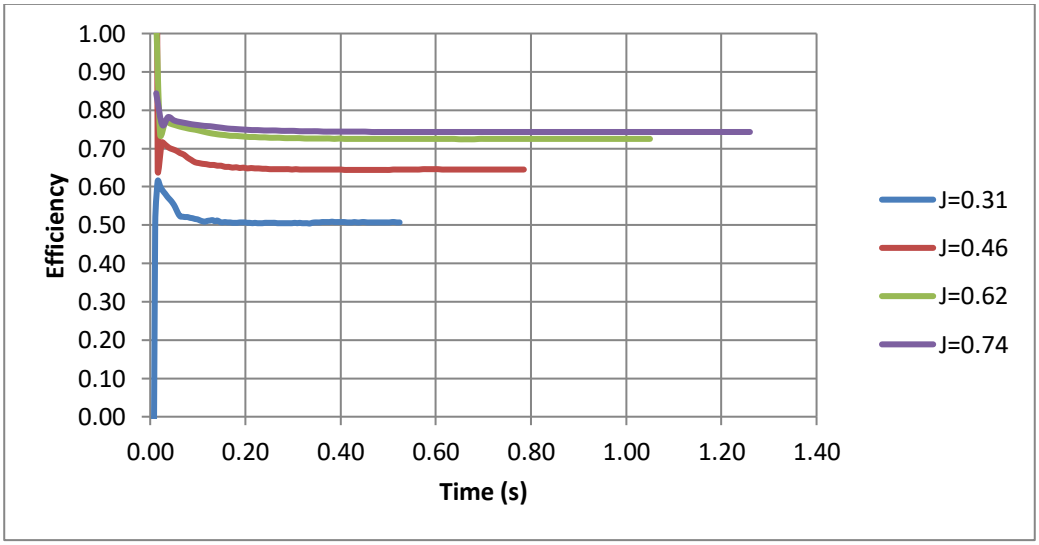

Figure 3-8: Efficiency as a function of time for an isolated propeller

The time independence of the solution is assessed using the propulsive efficiency; indeed time independence is achieved very quickly and thus a computation over five revolutions is deemed sufficient. Although Figure 3-8 shows only the evolution of efficiency in four advance ratios, the same behaviour is observed for all the other parameters. In order to estimate the performance parameters of the propeller, an average of the last two revolutions is considered.

Figure 3-9 and Figure 3-10 represent the variation of the thrust coefficients and torques coefficients with respect to the advance ratio respectively. In both figures are shown experimental [4] and computed results using OpenVSP. In both cases, the rotational speed is fixed at 3,000 RPM with the upstream velocity being varied accordingly in order to obtain the adequate advance ratios (yielding velocities ranging from 7.5 m/s to 31.5 m/s).

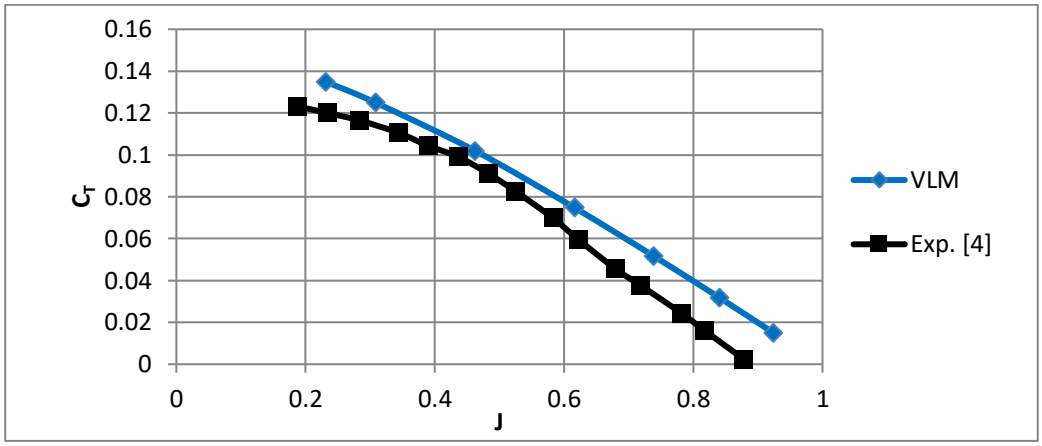

Figure 3-9: Thrust coefficint as a function of the advance ratio for an isolated propeller at 3,000 RPM

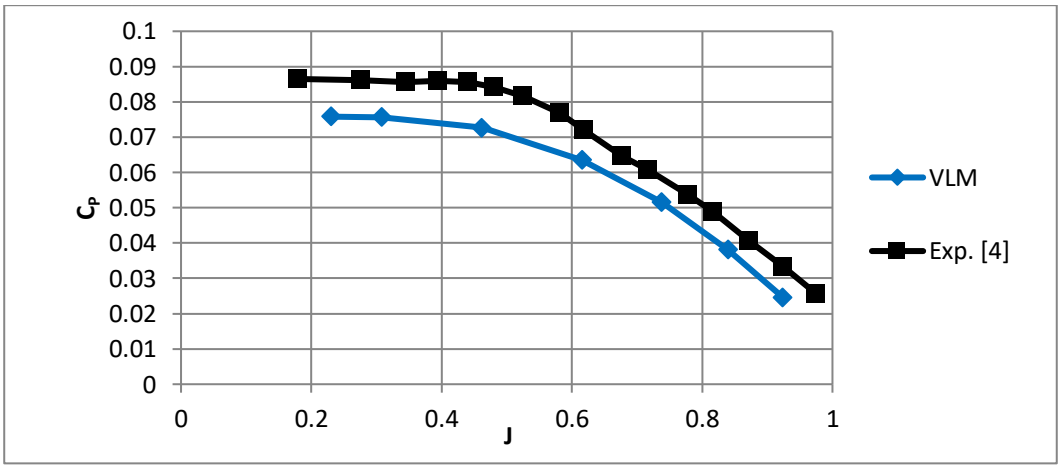

Figure 3-10: Torque coefficient as a function of the advance ratio for an isolated propeller at 3,000 RPM

Indeed, the same behaviour present in the work of Brandt and Selig [4] is predicted by VLM: values of C_T and C_P both decrease with the augmentation of the advance ratio. However, for a given value of J, the VLM consistently over-predicts the value of C_T and under-predicts the value of C_P.

The reason behind the differences between the values predicted by VLM and experimental results lies in the fact that the VLM considers the fluid as perfect with no

boundary layer model. Indeed, the loss of energy due to friction causes the thrust to be over-estimated and the power under-estimated.

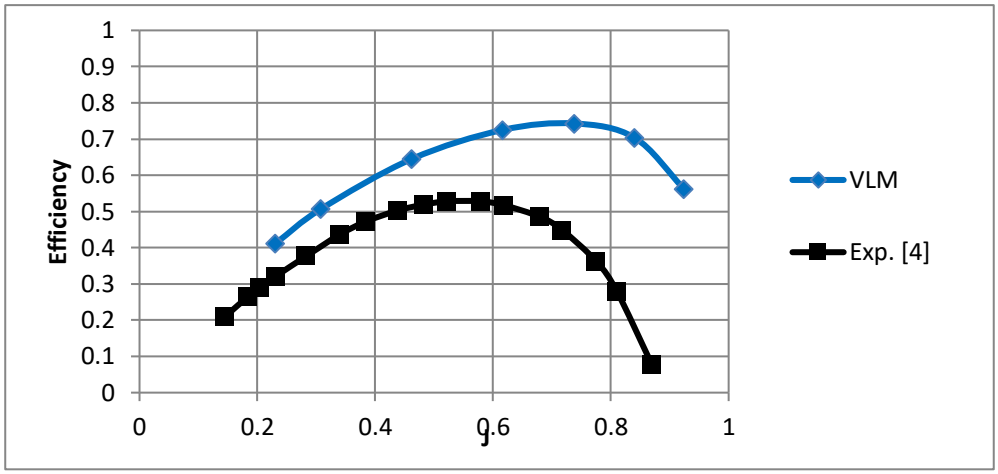

Figure 3-11: Propulsive efficiency as a function of the advance ratio for an isolated propeller at 3,000 RPM

Concerning the estimation of efficiency, results are completely different: the over-estimation of the C_T combined with the under-estimation of the C_P results in a large over-prediction of efficiency, especially on large advance ratios. Indeed at J=0.5, the efficiency is over predicted by at least 0.15, and at J=0.6 the difference is at around 0.2. The advance ratio corresponding to the maximum efficiency value is also over-estimated: around J=0.55 from experimental data, and J=0.75 from VLM.

Figure 3-12 depicts the variation of efficiency with the advance ratio for three different sets of cases (one where the RPM is fixed at 3,000 RPM, another with the RPM being 6,000 RPM, and finally a set of cases where the upstream velocity is fixed at 1 m/s corresponding to a range of 190 to 764 RPM). The calculations are performed in order to assess the consistency of the VLM method if the flow regime is changed.

The experimental results for efficiency [4] are shown on Figure 3-13: it is possible to observe that the efficiency decreases with the decrease of the RPM, indeed efficiency at J=0.6 decreases by around 0.05 when the RPM is reduced from 6,000 to 3,000 RPM. The decrease is efficiency is also predicted by VLM, but with a lower but non negligible extent: the efficiency loss is of only 0.01.

It is also interesting to note that the efficiency loss predicted between the 3,000 RPM set of cases and the 1 m/s (in which the RPM varies between 190 and 764 RPM) set is negligible.

Hence, these two sets of cases are considered to be equivalent, justifying the use of the 1 m/s set of cases for the rest of the present work.

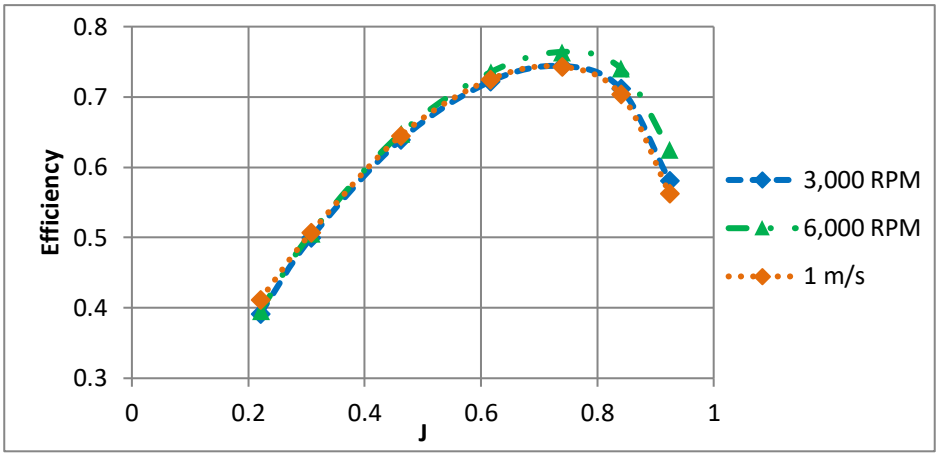

Figure 3-12: Efficiency as a function of the advance ratio for different regimes using VLM

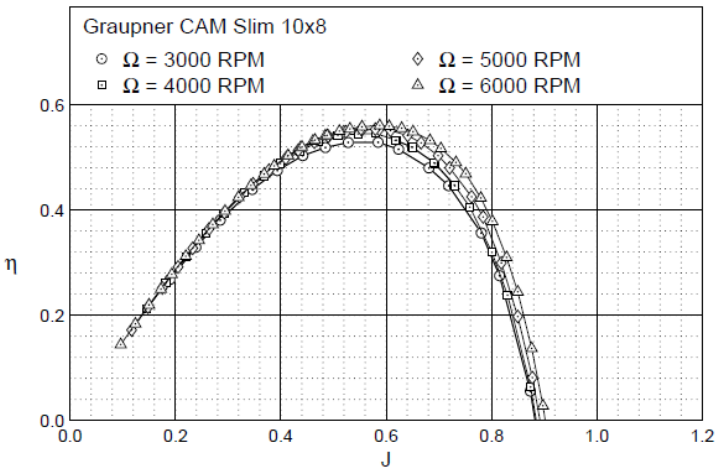

Figure 3-13: Efficiency as a function of the advance ratio for multiple rotational speed for the Graupner CAM Slim 10x8 [4]

3.3.2. Comparison for Equivalent Advance Ratios

Comparing the different configurations efficiencies considering equivalent advance ratios allows for a good assessment of performance in the same operating conditions; however it is important to note that these conditions are determined on design. In order to evaluate the performance of the CRP configurations, an average over the last two revolutions is taken to represent the sustained regime parameters.

A first observation common to all the computed parameters is that the values obtained in the CRP cases exhibit the same behaviour as the ones obtained for an isolated propeller.

It can be seen from Figure 3-14 that for the same advance ratio, the thrust coefficient of all CRP configurations is greater than the one of an isolated propeller. However, the difference between the two configurations reduces as advance ratios approach the value of 1.

The influence of inter-propeller distance is more pronounced for lower advance ratios (J=0.23; J=0.308), and becomes negligible for high advance ratios (J>0.462). The closer the two propellers are in a contra-rotating configuration, the higher the thrust coefficient.

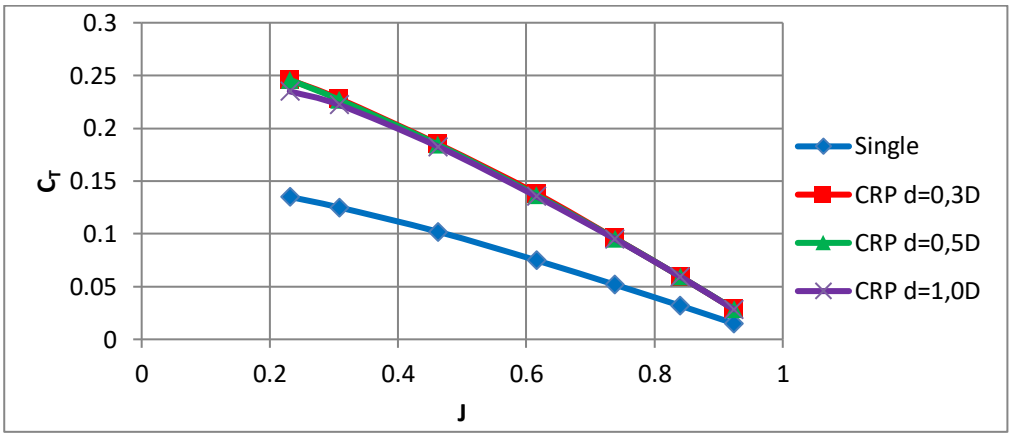

Figure 3-14: Thrust coefficient plot as a function of the advance ratio

Although CRP configurations produce higher values of C_T, they consume more power as can be observed from Figure 3-15 but the difference in power consumption reduces with the increase of the advance ratio. It can also be noted that the reduction of inter-propeller distance increases the power consumption for low advance ratios in a sensible way; however the effect of spacing becomes negligible as the value of J increases.

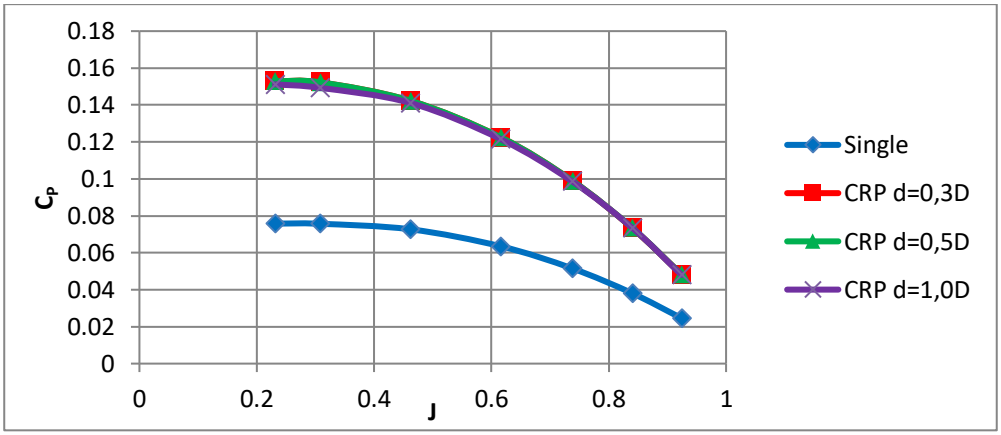

Figure 3-15: Power coefficient plot as a function of the advance ratio

Lastly, it can be observed from Figure 3-16, that for the same operating conditions (i.e. advance ratio), CRP systems are less effective. The difference in efficiency is significant (around 0.04) between the isolated propeller and CRP system.

The effect of inter-propeller distance on efficiency is further assessed in section 3.3.5.

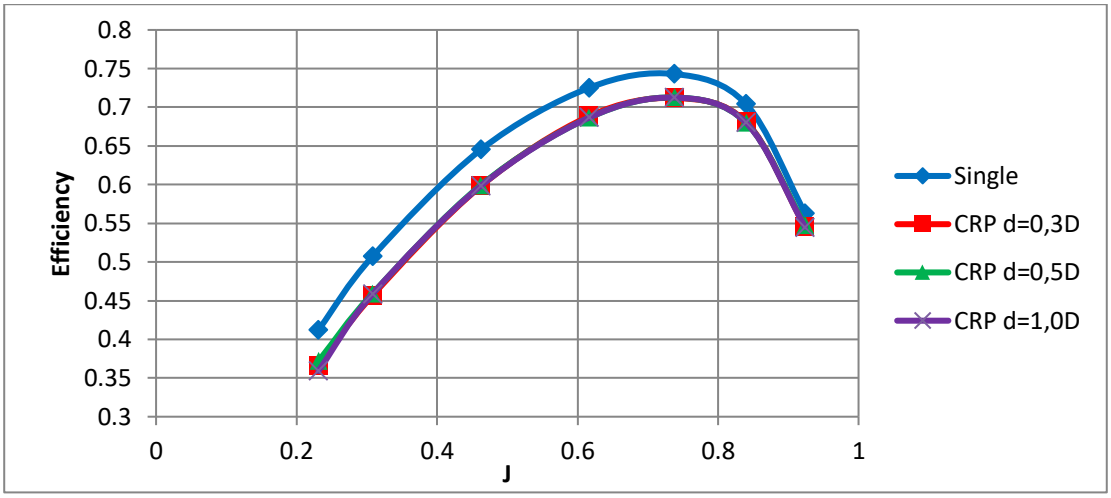

Figure 3-16: Efficiency plot as a function of the advance ratio

3.3.3. Comparison for Equivalent Thrust Coefficient

Comparing isolated and contra-rotating configurations for an equivalent thrust coefficient is a much more intuitive approach, and allows for the assessment of configurations with respect to design needs directly regardless of the advance ratio.

Multiple observations can be drawn from Figure 3-17 (it is important to note that values correspond to a decreasing arrangement of advance ratio, i.e. associated advance ratio decreases from left to right):

- The operational range of the CRP configuration is larger than the one of an isolated propeller;
- Although the maximal efficiency of an isolated propeller is higher than the one of the CRP configuration, it yields less thrust;
- For values of C_T less than 0.08 (zone 1), the efficiency of the isolated propeller is higher than the one of the CRP configuration;
- For values of C_T higher than 0.08 (zone 2), CRPs have a significantly higher efficiency than an isolated propeller;
- For equivalent values ofC_T, the advance ratio of the CRP configuration is higher than for the isolated propeller (this can be further confirmed by Figure 3-14).

This means that in zone 2, to produce and equivalent amount of thrust, CRPs not only have a higher efficiency, but also a smaller diameter (or a lower rotational speed) which decreases the loads on the propellers.

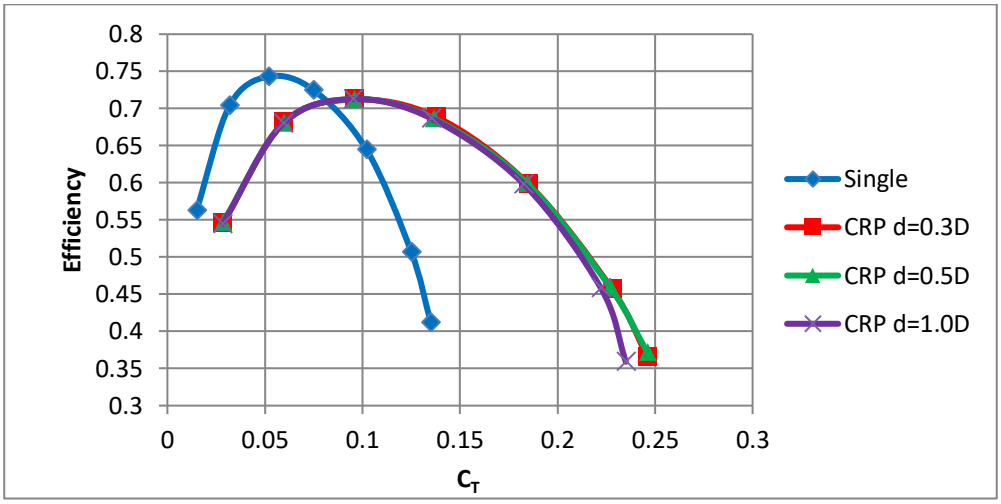

Figure 3-17: Efficiency plot as a function of the thrust coefficient

3.3.4. Comparison for Equivalent Power Coefficient

It is also possible to compare the two configurations for equivalent power coefficients (which is indicative of an equivalent power consumption/generation comparison). The same observations as in the previous section (3.3.3) can be made, namely that:

- The operational range of the CRP configuration is larger than the one of an isolated propeller;
- The maximal efficiency of an isolated propeller is higher than the one of the CRP configuration;
- For values of C_P less than 0.07 (zone 1), the efficiency of the isolated propeller is higher than the one of the CRP configuration;
- For values of C_P higher than 0.07 (zone 2), CRPs have a significantly higher efficiency than an isolated propeller;

For equivalent values ofC_P, the advance ratio of the CRP configuration is higher than for the isolated propeller, which means that in order to transfer the same amount of power to air (the surrounding fluid), CRPs require a smaller diameter (or a lower rotational speed).

Hence it can be said that CRP configurations are advantageous only when high values of power are needed; for systems requiring less power (and where power consumption is a more decisive factor than thrust), a single isolated propeller is more efficient.

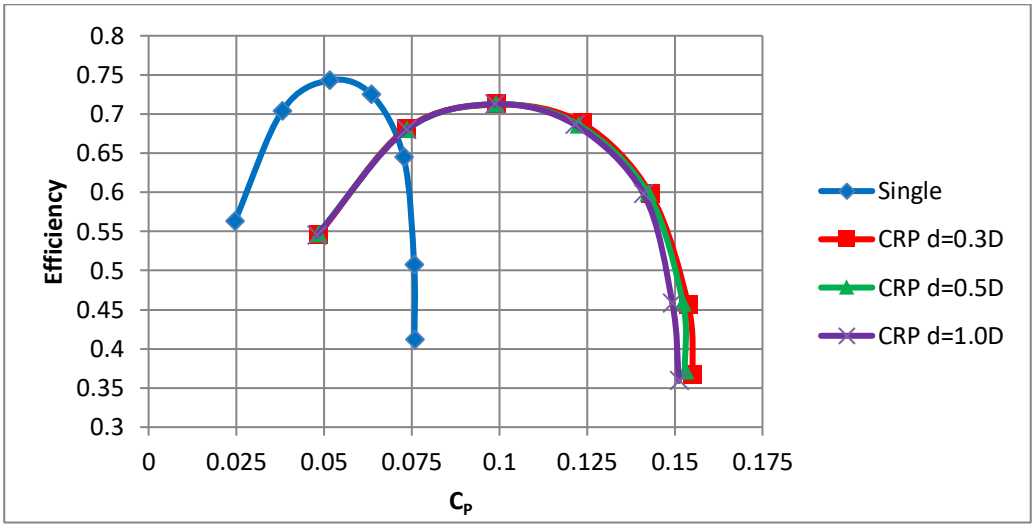

Figure 3-18: Efficiency plot as a function of the power coefficient

3.3.5. INTER-PROPELLER DISTANCE EFFECTS

Although results are not expected to be in line with experimental data concerning efficiency, it is still possible to evaluate the performances of CRP systems from a qualitative point of view using VLM and compare them with the isolated propeller case (also, computed using VLM). Below are presented unsteady results (C_T and C_P only) for an advance ratio of J=0.616 for different inter-propeller distances.

The unsteady nature of the CRP systems is quite visible in the following plots, and the question of loading on the blades could be discussed, however, as results are not quantitatively applicable, an analysis of the variation of thrust (represented by C_T) and power (represented by C_P) is deemed sufficient.

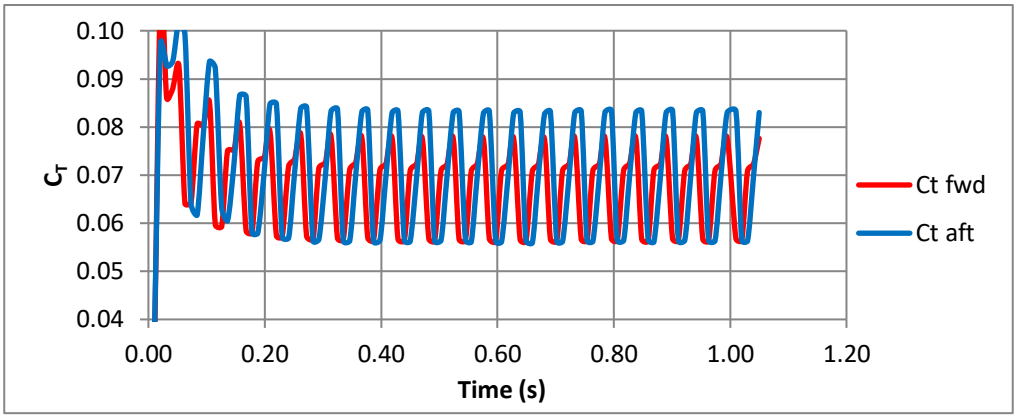

Figure 3-19: Instantaneous thrust coefficient for a spacing of 0.1D

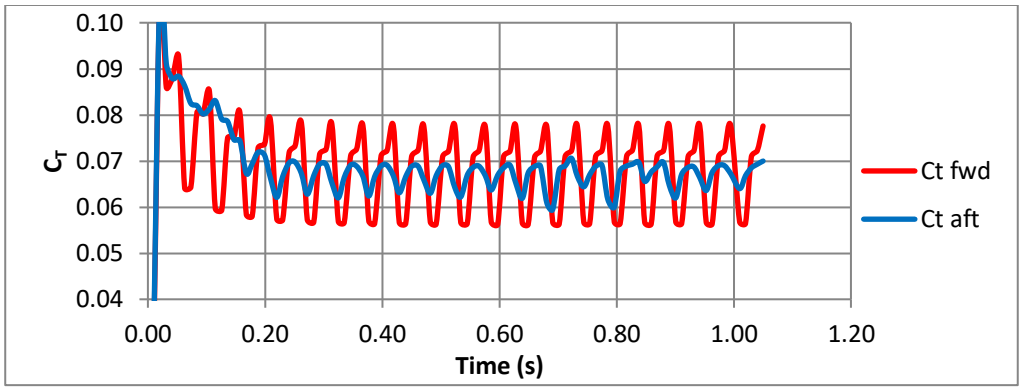

Figure 3-20: Instantaneous thrust coefficient for a spacing of 0.3D

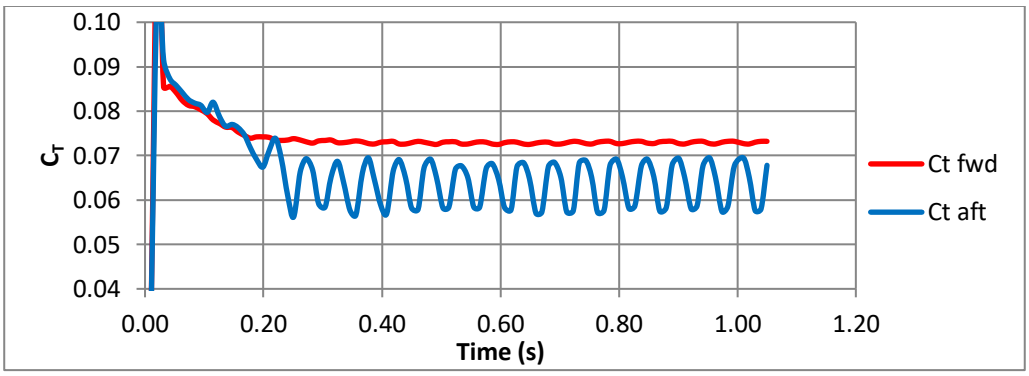

Figure 3-21: Instantaneous thrust coefficient for a spacing of 0.5D

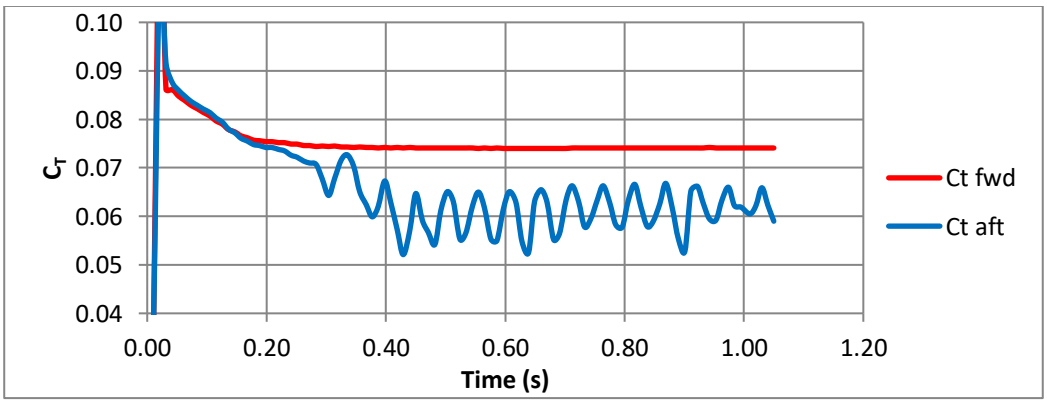

Figure 3-22: Instantaneous thrust coefficient for a spacing of 1.0D

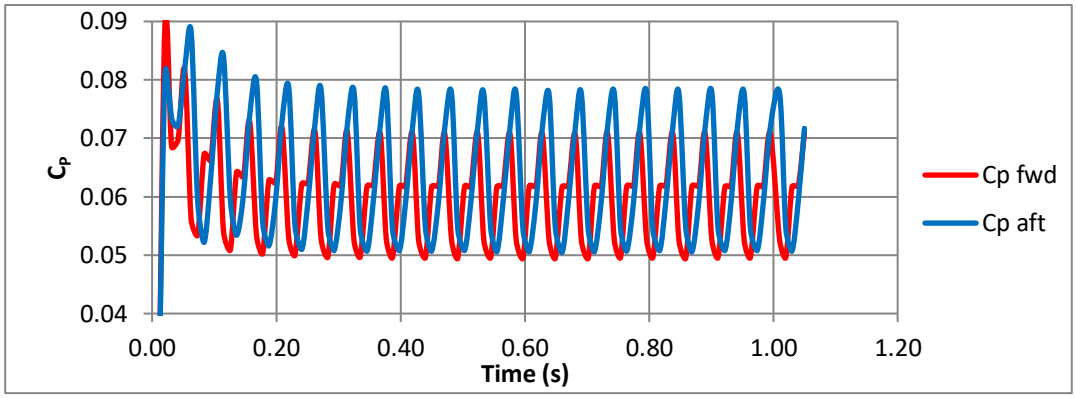

Figure 3-23: Instantaneous power coefficient for a spacing of 0.1D

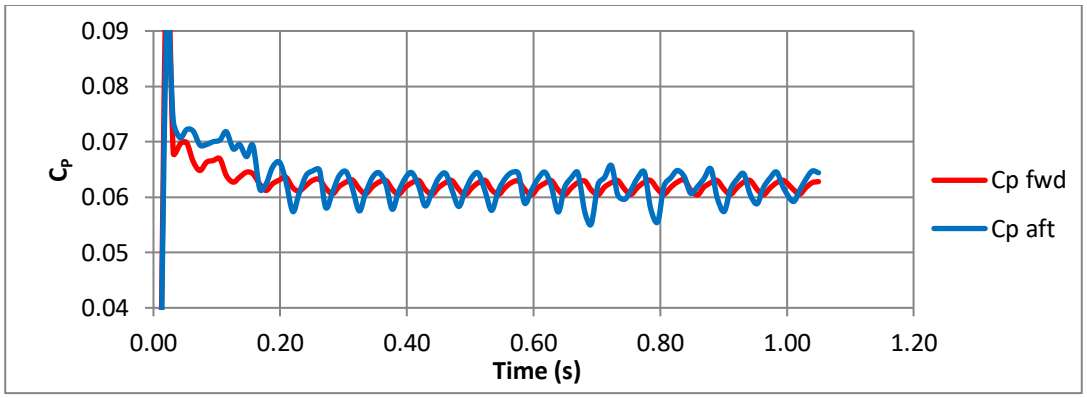

Figure 3-24: Instantaneous power coefficient for a spacing of 0.3D

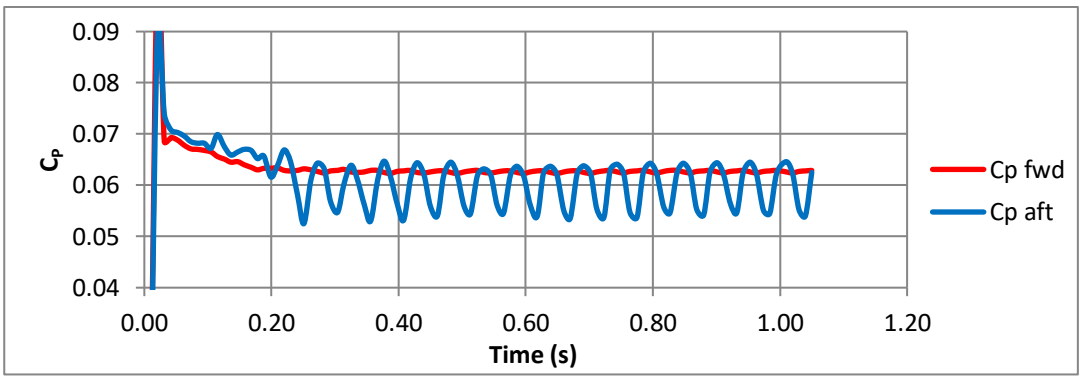

Figure 3-25: Instantaneous power coefficient for a spacing of 0.5D

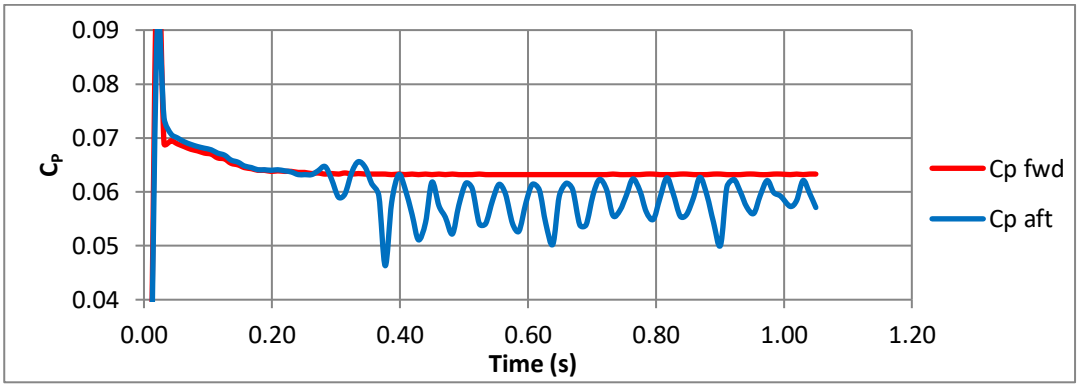

Figure 3-26: Instantaneous power coefficient for a spacing of 1.0D

The figures above represent the variation of the thrust and power coefficients over time for four different inter-propeller distances; the instantaneous performance of the CRP configurations in terms of thrust and power is greatly dependent on spacing. It is also important to note that although the flow is intrinsically unsteady a sustained flow regime is achieved by the first or second revolution of the propeller (the time taking to attain this regime increasing as the distance between the propellers increases). Table 3-1 provides a comprehensive summary of the above figures (amp refers to the amplitude). The period is almost equal in all cases (variations are due to numerical errors), at about 0.05s: each oscillation period corresponding to one quarter of a rotation which is when the forward and afterward blades "meet" when looked upon from the front/rear.

Table 3-1: Values of C_T and C_P for different CRP configurations

Spacing	C_T ($\times 10^3$)						C_P ($\times 10^3$)					
	fwd			aft			fwd			aft		
	max	min	amp	max	min	amp	max	min	amp	max	min	amp
d=0.1D	78	55	23	85	55	30	71	49	22	78	51	27
d=0.3D	78	55	23	69	64	5	63	60.5	2.5	65	58	7
d=0.5D	73	72	1	70	57	12.5	63	62	1	64.5	53.5	11
d=1.0D	74	74	~0	67	52	N/A	63.5	63.5	~0	62.5	55	N/A

It is also possible to observe the following:

- For a distance of 0.1D: the values of C_T and C_P oscillate with high amplitudes. For both C_T and C_P the amplitude of the aft propeller is larger than that of the front.
- For a distance of 0.3D: the oscillations are still present for both parameters, however there are differences between the behaviour of the C_T and C_P. For the thrust coefficient, the amplitude of the oscillations of the aft propeller diminished by a considerable amount whereas the oscillations of the fwd propeller remain identical, making the oscillations of the fwd larger than the ones of the aft. Concerning the C_P, the amplitudes of both propellers diminish greatly, but the aft propeller stills shows higher values of amplitude.
- For a distance of 0.5D: C_T and C_P show similar unsteady behaviours. Indeed, the fwd propeller is subject to very small (but noticeable) oscillations of both performance parameters, as for the aft propeller oscillations with amplitude similar to the 0.3D distance case can be observed. Overall, the average values of the C_T and C_P of the aft propeller are lower than those of the fwd one.

- For a distance of 1.0D: C_T and C_P show similar unsteady behaviours. For the fwd propeller, the values are constant, whereas the aft propeller values oscillate with a consistent frequency but and an irregular amplitude.

Another observation which is common to all the studied quantities is that the frequency of the oscillations is identical, and is directly related to the rotational frequency of the propellers (the number of revolutions per second) with the spacing having little to no effect. Indeed, to each revolution of the CRPs, correspond four oscillations: the period of the oscillations is ¼ of the CRP period, meaning the frequency φ is equal to:

$$\varphi = 4 \times N \tag{4.4}$$

It is important to note that the oscillations are consequence of the time periodicity of the geometry found in turbomachinery (and not flow turbulence), which in the studied case (of same diameter, number of blades and RPM of the fwd and aft propellers) is straightforward to predict.

Although the oscillations are not turbulence induced, it is possible to define a Strouhal number for the studied configurations as follows:

$$St = \frac{\varphi c_{ref}}{U_b} = \frac{4Nc_{ref}}{\frac{3}{4}\frac{D}{2}2\pi N} = \frac{16c_{ref}}{3\pi D} \tag{4.5}$$

With:

- U_b: velocity of the blade at the reference chord

This yields in the studied cases a Strouhal number of:

$$St \cong 0.142$$

The obtained Strouhal number is a constant in this specific type of CRPs (same geometry and RPM) and can be considered low enough to justify a performance study using the average quantities.

In order to assess the effect of spacing on performance, the relative efficiency gain is discussed, with the efficiency being the average efficiency over the last two revolutions.

Table 3-2: Efficiency for CRP configurations at different advance ratios

Advance ratio (J)	Efficiency					Maximal Efficiency gain from d=1.0D	Maximal Relative gain from d=1.0D
	d=0.08D	d=0.1D	d=0.3D	d=0.5D	d=1.0D		
0.23	0.362	0.364	0.366	0.372	0.359	7.12e-3	1.26%
0.31	0.452	0.453	0.457	0.459	0.458	6.78e-4	0.15%
0.46	0.595	0.601	0.598	0.599	0.598	2.58e-3	0.43%
0.62	0.690	0.688	0.688	0.686	0.686	1.88e-3	0.47%
0.74	0.716	0.715	0.712	0.713	0.713	2.27e-3	0.31%

Table 3-2 illustrates the efficiency for five difference CRP configurations at different advance ratios. The largest distance (d=1.0D) is taken as reference; efficiency gain is assessed relative to the reference distance. Hence, positive values correspond to a relative increase in efficiency with respect to the reference case. This choice of reference is purely arbitrary and serves only an illustration purpose. It s possible to observe that the effect of inter-propeller distance on efficiency is negligible, except for the smallest advance ratio of J=0.23 for which the maximal gain is of 1.26%. However, the change in inter-propeller distance is predicted to have an effect on the thrust coefficient for low advance ratio. Indeed, for the advance ratio corresponding to the maximal efficiency, the effect of spacing is negligible.

Table 3-3: Thrust coefficient for CRP configurations at different advance ratios

Advance ratio (J)	Thrust coefficient					Maximal C_T gain from d=1.0D	Maximal Relative gain from d=1.0D
	d=0.08D	d=0.1D	d=0.3D	d=0.5D	d=1.0D		
0.23	0.247	0.248	0.246	0.246	0.235	13e-3	5.5%
0.31	0.228	0.227	0.228	0.227	0.222	5.8e-3	2.6%
0.46	0.187	0.186	0.185	0.185	0.182	4.7e-3	2.6%
0.62	0.138	0.137	0.138	0.137	0.135	2.7e-3	1.9%
0.74	0.096	0.0956	0.0958	0.0956	0.0952	0.8e-3	0.8%

This leads to the conclusion that unless the CRP configuration is expected to operate at low advance ratios (which is highly unlikely as simple propellers perform better in this range), spacing between the propeller has negligible effects on the average performance. Hence, choice of the inter-propeller distance is expected to be based on the amplitude of the oscillations of the thrust and power coefficients rather than their average values.

CHAPTER 4:
COMPUTATIONAL FLUID DYNAMICS SIMULATIONS

CHAPTER 4: COMPUTATIONAL FLUID DYNAMICS SIMULATIONS

Computational fluid dynamics simulations are performed using the open source software OpenFOAM using the sliding mesh technique. However, the grid independence study is performed using ANSYS Fluent using MRF (Multiple Reference Frame) because of the more straightforward (and less time consuming) procedure that allows to test multiple grid in more reduced amount of time.

4.1. MATHEMATICAL FORMULATION

4.1.1. GOVERNING EQUATIONS

The equations governing the motion of fluids are the Navier-Stokes equations which can be thought as either conservation equations or transport equations. As the current study treats only the incompressible regime case, the governing equations are the continuity equation (conservation/transport of mass) and the momentum equation (conservation/transport of momentum) shown below (in Cartesian coordinates):

$$\frac{\partial \rho}{\partial t} + \left[\frac{\partial(\rho u)}{\partial x} + \frac{\partial(\rho v)}{\partial y} + \frac{\partial(\rho w)}{\partial z}\right] = 0 \tag{5.1}$$

$$\begin{cases} \dfrac{\partial u}{\partial t} + u\dfrac{\partial u}{\partial x} + v\dfrac{\partial u}{\partial y} + w\dfrac{\partial u}{\partial z} = -\dfrac{1}{\rho}\dfrac{\partial p}{\partial x} + \dfrac{\mu}{\rho}\left(\dfrac{\partial^2 u}{\partial x^2} + \dfrac{\partial^2 u}{\partial y^2} + \dfrac{\partial^2 u}{\partial z^2}\right) + f_x \\ \dfrac{\partial v}{\partial t} + u\dfrac{\partial v}{\partial x} + v\dfrac{\partial v}{\partial y} + w\dfrac{\partial v}{\partial z} = -\dfrac{1}{\rho}\dfrac{\partial p}{\partial y} + \dfrac{\mu}{\rho}\left(\dfrac{\partial^2 v}{\partial x^2} + \dfrac{\partial^2 v}{\partial y^2} + \dfrac{\partial^2 v}{\partial z^2}\right) + f_y \\ \dfrac{\partial w}{\partial t} + u\dfrac{\partial w}{\partial x} + v\dfrac{\partial w}{\partial y} + w\dfrac{\partial w}{\partial z} = -\dfrac{1}{\rho}\dfrac{\partial p}{\partial z} + \dfrac{\mu}{\rho}\left(\dfrac{\partial^2 w}{\partial x^2} + \dfrac{\partial^2 w}{\partial y^2} + \dfrac{\partial^2 w}{\partial z^2}\right) + f_z \end{cases} \tag{5.2}$$

With:

- $x; y; z$: spatial variables;
- $u; v; w$: components of the velocity in the $x; y; z$ directions respectively;
- $f_x;\ f_y;\ f_z$: volume forces acting on the fluid in the $x; y; z$ directions respectively;
- p : pressure;
- ρ : fluid density;
- μ : fluid dynamic viscosity.

As an incompressible case without temperature variations is considered, the field dependent variables are u, v, w and P, whereas density and dynamic viscosity are taken as

constants ($\mu = 1.789 \times 10^{-5}\ Pa.s$ and $\rho = 1.225\ kg/m^3$ for air at sea level conditions), with volume forces (gravity) being neglected.

4.1.2. REYNOLDS AVERAGING

The most feasible way of simulating flows, is to model all turbulence and solving for the mean flow; this is done by using the Reynolds Averaged Navier-Stokes (RANS) approach. In this case, the parameters in the governing equations are averaged over a characteristic time interval Δt in order to eliminate the influence of turbulent fluctuations, meanwhile the unsteadiness of the other physical phenomena is preserved [1]. In the equation below, a nondescript quantity $A(x_i, t)$ is represented.

$$A(x_i, t) = \bar{A}(x_i) + A'(x_i, t) \tag{5.3}$$

The mean value $\bar{A}(x_i)$ being calculated as follows:

$$\bar{A}(x_i) = \frac{1}{\Delta t}\int_t^{t+\Delta t} A(x_i, t)\, dt \tag{5.4}$$

With:

- $A(x_i, t)$: a nondescript quantity;
- $\bar{A}(x_i)$: averaged quantity A over a characteristic time;
- $A'(x_i, t)$: fluctuation of quantity A;
- t: time variable;
- Δt: characteristic time interval.

The resulting equations from this averaging process are identical to the original except with the addition of a new term in the momentum equations, called the Reynolds stress tensor. The averaged momentum equations are written in tensor form for the sake of simplicity with R_{ij} being the Reynolds stress tensor.

$$\rho\left(\frac{\partial \overline{u_i}}{\partial t} + \overline{u_k}\frac{\partial \overline{u_i}}{\partial x_k}\right) = -\frac{\partial \bar{P}}{\partial x_i} + \frac{\partial}{\partial x_j}\left(\mu\frac{\partial \overline{u_i}}{\partial x_j}\right) + \frac{\partial}{\partial x_j}R_{ij} \tag{5.5}$$

With: $R_{ij} = -\rho\overline{u_i' u_j'}$

The addition of this new term poses a closure problem on the system since the Reynolds stress tensor adds six new unknown variables.

4.1.3. TURBULENCE MODELLING

There are many options in providing the closure process: zero-equation (algebraic) models, one-equation models, two-equation models, second order closure (Reynolds stress) models and algebraic stress models can be applied to incompressible flows [5].

In the present work, the two-equation $k-\varepsilon$ model [11] is used to close the system. The model uses the Boussiquet theorem (or the idea of eddy/turbulent viscosityμ_T) to compute the Reynolds stress tensor.

$$R_{ij} = -\rho\overline{u_i'u_j'} = \mu_T\left(\frac{\partial\overline{u_i}}{\partial x_j}+\frac{\partial\overline{u_j}}{\partial x_i}\right)-\frac{2}{3}\mu_T\frac{\partial\overline{u_k}}{\partial x_k}\delta_{ij}-\frac{2}{3}\rho k\delta_{ij} \tag{5.6}$$

The specificity of the $k-\varepsilon$ model is that it uses the turbulent kinetic energy k and turbulent dissipation rate ε to determine the eddy viscosity as shown by equation (5.6):

$$k = \frac{1}{2}\overline{u_\iota u_\iota} \tag{5.7}$$

$$\varepsilon = \frac{\mu}{\rho}\overline{\frac{\partial u_\iota}{\partial x_k}\frac{\partial u_\iota}{\partial x_k}} \tag{5.8}$$

$$\mu_T = \rho C_\mu\frac{\bar{k}^2}{\bar{\varepsilon}} \tag{5.9}$$

With k and ε being determined using the following transport equations:

$$\frac{D\varepsilon}{Dt} = \frac{1}{\rho}\frac{\partial}{\partial x_k}\left[\frac{\mu_t}{\sigma_\varepsilon}\frac{\partial\varepsilon}{\partial x_k}\right]+\frac{C_1\mu_t}{\rho}\frac{\varepsilon}{k}\left(\frac{\partial u_i}{\partial x_k}+\frac{\partial u_k}{\partial x_i}\right)\frac{\partial u_i}{\partial x_k}-C_2\frac{\varepsilon^2}{k} \tag{5.10}$$

$$\frac{Dk}{Dt} = \frac{1}{\rho}\frac{\partial}{\partial x_k}\left[\frac{\mu_t}{\sigma_k}\frac{\partial k}{\partial x_k}\right]+\frac{\mu_t}{\rho}\left(\frac{\partial u_i}{\partial x_k}+\frac{\partial u_k}{\partial x_i}\right)\frac{\partial u_i}{\partial x_k}-\varepsilon \tag{5.11}$$

With:

- $C_\mu = 0.09$;
- $C_1 = 1.44$;
- $C_2 = 1.92$;
- $\sigma_k = 1.0$;
- $\sigma_\varepsilon = 1.2$;

The model above is representative of a fully turbulent flow; however that is not the case near walls. One method to take into account the influence of nearby walls is to use wall functions. This method has two advantages: firstly, it allows for shorter computational times and less storage memory use; and secondly, empirical information can be added to wall

functions in order to take into account roughness. The wall function used in this method is the following, for the momentum flux:

$$\frac{U_P}{\left(\tau/\rho\right)_W} C_\mu^{1/4} k_P^{1/2} = \frac{1}{\kappa} \ln\left[E y_P \frac{\mu C_\mu^{1/4} k_P^{1/2}}{\rho}\right] \tag{5.12}$$

With values with subscript W being the values at the wall, while the ones with subscript P being the ones at the first computational point starting from the wall:

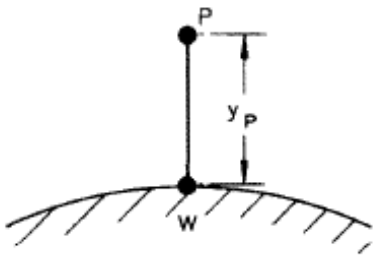

Figure 4-1: Near-wall node [11]

- y_P: the distance between point P and the wall
- E: a function of wall roughness (about 9.0 for a smooth wall)
- κ: Von Karman constant
- τ: shear stress

4.2. NUMERICAL APPROACH

4.2.1. FINITE VOLUME METHOD

The most popular method in CFD is the finite volume method (or FVM) which is used in roughly 80% of commercial codes [1].

The FVM was originally introduced by McDonald in 1971 [1]. The computational domain is divided into cells (or finite volumes), with the flow field variables being evaluated in the centre points of each cell and are interpreted as the average values of their respective cell. The advantage of the FVM lies in the fact that the method is independent of cell shape and location which allows for more flexibility in the grid generation process [1].

A throughout explanation of the FVM can be found in the work of Chung [5] and Árpád & József [1], however only a general idea about the method is shown in the present thesis.

The conservative form of the governing equations is used in this method:

$$\frac{\partial U}{\partial t}+\frac{\partial F_i}{\partial x_i}+\frac{\partial G_i}{\partial x_i}=B \tag{5.13}$$

The finite volume equations are obtained (with R being the residual and Ω being the control volume) as:

$$\int_{\Omega} R d\Omega=\int_{\Omega}\left(\frac{\partial U}{\partial t}+\frac{\partial F_i}{\partial x_i}+\frac{\partial G_i}{\partial x_i}-B\right)d\Omega=0 \tag{5.14}$$

Using the divergence theorem, it follows:

$$\frac{\partial}{\partial t}\int_{\Omega} U d\Omega+\int_{\Gamma}(F_i+G_i)n_i d\,\Gamma+\int_{\Omega} B d\Omega=0 \tag{5.15}$$

With:

- Γ: control surface
- n_i: component of unit vector normal to the control surface

In order to pass from a continuous space to a discreet space, variable U in a cell is considered as equal to the average of that value (Only a two-dimensional case is shown for illustration purposes):

$$A_{ij}=\frac{1}{\Omega_{i,j}}\int_{\Omega} A d\Omega \tag{5.16}$$

With:

- i: index of the cell in the x direction;
- j: index of the cell in the y direction;

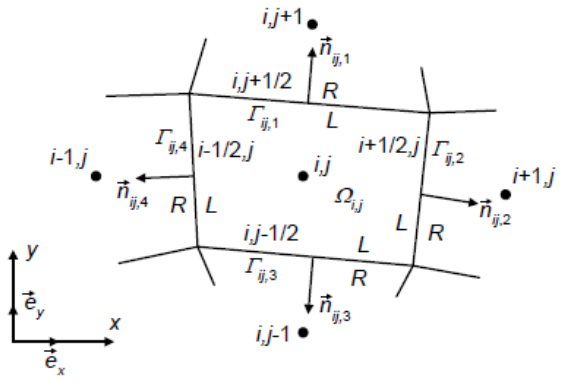

Figure 4-2: Cell-centered quadrilateral finite volume [1]

In the scope of this work $B=\begin{bmatrix}0\\0\end{bmatrix}$, hence it is possible to obtain the following semi-discreet expression which can then be solved numerically:

$$\frac{d}{dt}U_{ij} = -\frac{1}{\Omega_{i,j}}\left(\sum_{k=1}^{N_b}\left[\left(F_{ij,k} + G_{ij,k}\right)n_{ij,k}\Gamma_{ij,k}\right]\right) = \Re_{i,j} \tag{5.17}$$

With:

- N_b: number of boundaries in the cell of interest;
- i, j: indices of the cell of interest in the x and y directions respectively;
- $\Re_{i,j}$: residual.

4.2.2. USED MACHINES

Grid independence study is performed using the machines available at the Laboratory of Aeronautical Sciences (LSA) at the Institute of Aeronautics and Space Studies (University of Saâd Dahleb Blida 1), while the actual test cases are performed using a workstation at the Wind Energy Division of the Renewable Energies Development Centre (CDER), located at Ben Aknoun, Algiers. The machines have the following specifications:

Table 4-1: Used machines specifications

	Machine 1	Machine 2	Machine 3
Location	CDER	LSA	LSA
Processor name	Intel i7 10700H	Intel Xeon E5-1650 v2	Intel Xeon E5-2620 v4
Processor clock speed	2.90 GHz	3.50 GHz	2.10 GHz
Processor cores	8	6	8
Processor threads	16	12	16
RAM	32 GB	128 GB	128 GB

4.2.3. GEOMETRY GENERATION

The computational domain is generated using Gambit v 2.4.6 which is a software under the ANSYS umbrella that allows to create geometries as well as computational grids.

The domain consists in a cylinder split into two sub-domains for the isolated propeller case, and into three sub-domains for the CRP configuration cases. The propeller itself is the same as specified in section 3.2.2, the hub of the propeller is neglected for meshing considerations, so only blade effects are taken into account.

In the following two dimensionless representations of the computational domains, the unit length of 1 corresponds to the propeller diameter, with the fwd propeller being placed at the origin, the representations below ought to be imagined as a slice of a cylinder at the plane corresponding to z=0. The choice of the domain dimensions is done according to reference [2].

It is important to note that the x axis is in the direction of the flow velocity, hence the left face of the domain (in Figure 4-3 and Figure 4-4) is the inlet and the right face the outlet, the bottom/top face is supposed to be in the far field. Each blade is its own named selection, thus blades are named from "blade1" and "blade2" (or "blade1" to "blade4" in the CRP configuration). For the isolated propeller case, only two interfaces have to be set which are named "interface_R-S" and "interface_S-R", for the CRP configurations with spacings of 0.5D and 1.0D four interfaces have to be set ("interface_R1-S", "interface_S-R1", "interface_R2-S" and "interface_S-R2"), and as for the CRP configuration with a spacing of 0.3D six interfaces have to be set ("interface_R1-S", "interface_S-R1", "interface_R2-S", "interface_S-R2", "interface_R1-R2" and "interface_R2-R1").

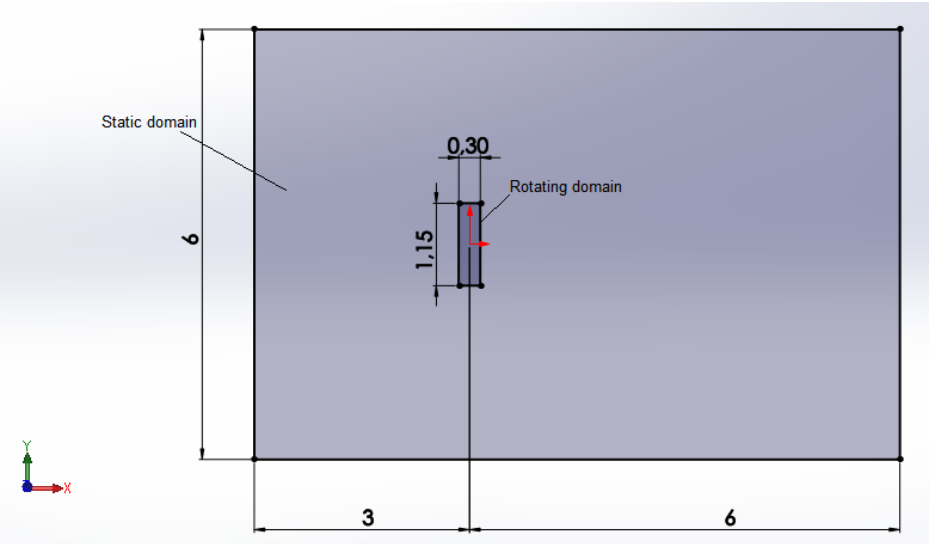

Figure 4-3: Slice of the computational domain of the isolated propeller case

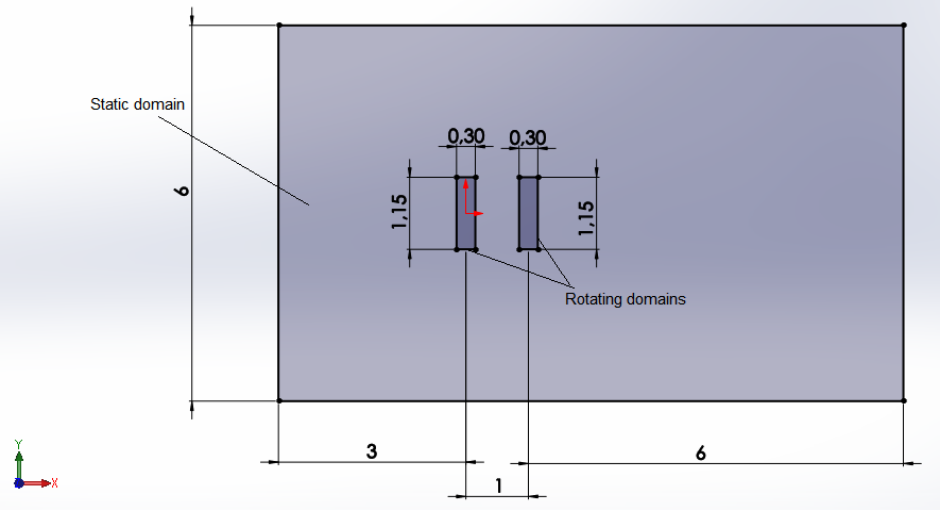

Figure 4-4: Slice of the computational domain for the CRP case with inter-rotor distance of 1D

4.2.4. COMPUTATIONAL GRID

In this section, only a qualitative description of the computational grids for the static and rotating domains is addressed. A more statistical description is given in section 0.

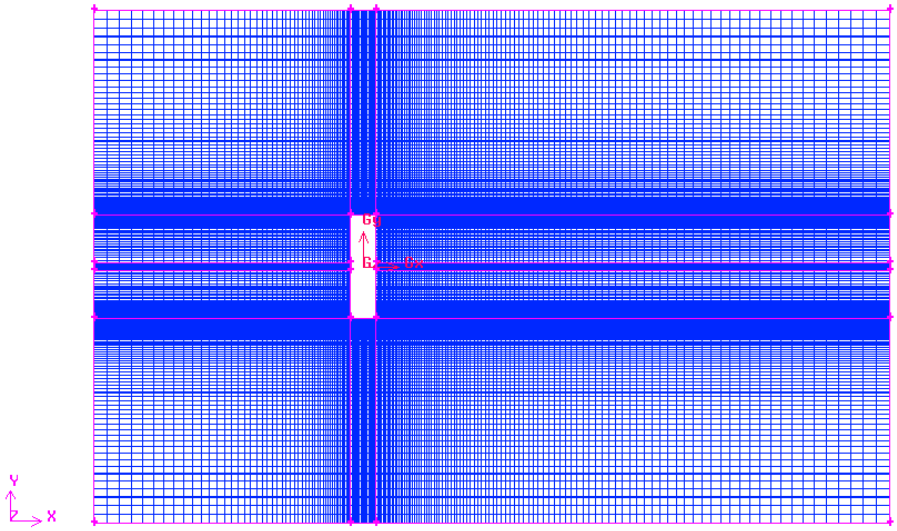

Figure 4-5: Slice of the computational grid of the static domain at z=0

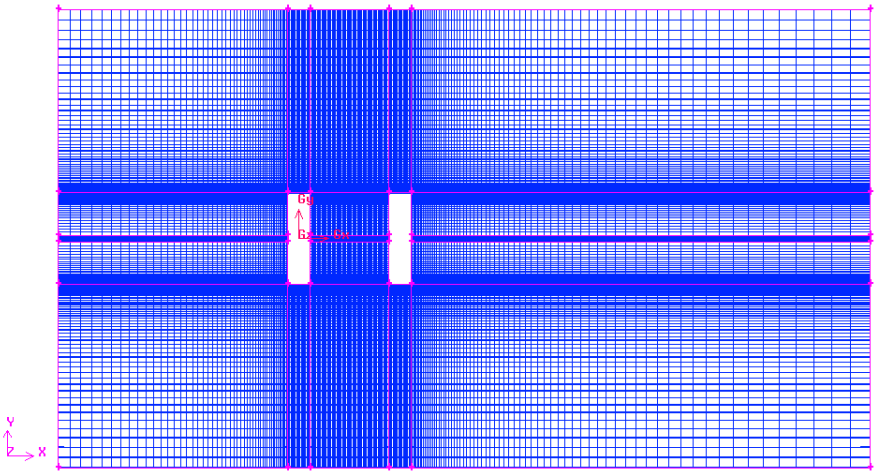

Figure 4-6: Slice of the computational grid of the static domain for the CRP configuration

In the static domain, a fully structured hexahedral grid is used. The grid is refined at the rotating domain proximity with an emphasis put on the radial interface between them. Figure 4-5 represents a slice of the cylindrical static domain at the plane z=0.

For the CRP configurations, a slice at the plane corresponding to z=0 is shown in Figure 4-6. The grid is particularly refined in the inter-propeller region in order to capture any interaction influencing performance.

However, in the rotating domain a hybrid approach is adopted, in the vicinity of the blades as well as the radial interface, a fully structured hexahedral grid is used with the value of y+ being kept between 30 and 140 for all cases. In the rest of the domain tetrahedral cells are adopted. The following figures (Figure 4-7, Figure 4-8, Figure 4-9) are slices of the rotational domain.

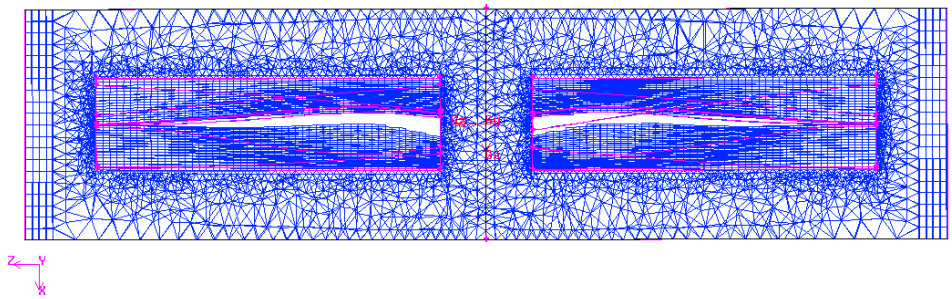

Figure 4-7: Slice of the computational grid of the rotating domain at y=0

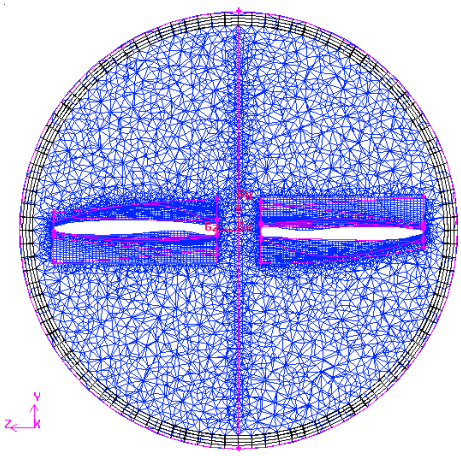

Figure 4-8: Slice of the computational grid of the rotating domain at x=0

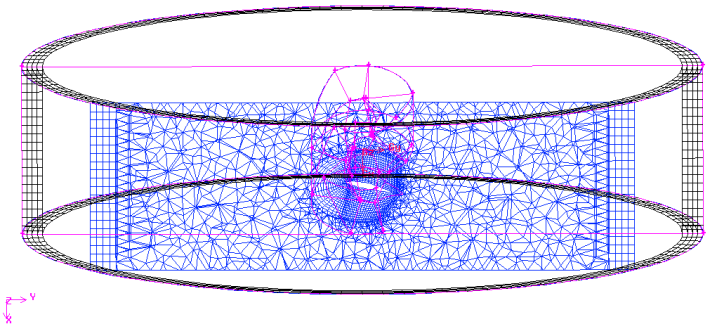

Figure 4-9: Slice of the computational grid of the rotating domain at 0.75R

4.2.5. SIMULATION CASE SET-UP WITH OPENFOAM

OpenFOAM (standing for Open Field Operation And Manipulation) is the most popular open-source software for computational fluid dynamics and is available under the General Public Licence (GPL). This software was created in 1989 by Henry Weller under the name "FOAM" and was released open-source by him, Chris Greenshields and Mattijs Janssens in 2004 [23]. For the present project, an Ubuntu installation of the OpenFOAM 7 version is used.

OpenFOAM does not include a GUI, hence setting up a CFD case consists in directly modifying the case files and executing commands on the terminal. An OpenFOAM case directory (or folder) contains three sub-directories, namely: "0", "constant" and "system" described below:

- "0": contains the boundary and initial conditions;
- "constant": contains the initial computational grid, as well as the dynamic mesh dictionary and the turbulence model settings;
- "system": contains all the solver related settings, namely; residual control, numerical schemes, time step control, parallel decomposition and forces calculations.

4.2.5.1. Computational grid import procedure:

As OpenFOAM does not contain a GUI, some directory manipulation and a set of commands must be done to exploit the Gambit grid. It is important to note that the computational grid must be exported in the ".neu" format for OpenFOAM to accept it, and two separate grids for the stator and rotor have to be generated. The following steps must be followed in order to import and merge the grids:

- Step 1: create two case directories which are named "rotor" and "stator" (these can be obtained from any tutorial case);
- Step 2: copy the .neu computational grids into the /rotor/ and /stator/ directories respectively;
- Step 3: open a terminal and execute the "run" command;
- Step 4: access the stator directory, with the command "cd theFolderPath";
- Step 5: convert the .neu grid to an OpenFOAM polyMesh grid with the command: "gambitToFoamnameOfTheGrid.neu";

- Step 6: repeat steps 4 and 5 for the rotor grid (to back up one level, the command is “cd ../”);
- Step 7: execute the “pwd” command which indicates the current directory full path;
- Step 8: execute the command “mergeMeshesfullPathForRotorfullPathForStator”
- Step 9: move the new imported and merged grid to the constant directory of the intended case, and properly modify the polyMesh/boundary file;
- Step 10: create a rotating domain with the following commands: “setSet”; “cellSet c0 new cylinderToCell (x_1 0 0) (x_2 0 0) 0.2”; “cellZoneSet c0Zone new setToCellZonec0”; “quit”.

The same procedure is applicable for the CRP configuration but with an additional grid to import and merge, and creating another rotating domain.

4.2.5.2. “0” directory settings:

The boundary and initial conditions are summarized in the following table (patches correspond to named selections), the “internalField” line corresponds to the initial conditions and “fixedValue” corresponds to a user specified value. Actual values are adjusted to obtain the adequate advance ratios.

Table 4-2: Boundary conditions

Patches	U	P	Nut	k	Eps
Internal Field	uniform	uniform	uniform	uniform	uniform
inlet	fixedValue	zeroGradient	Calculated	fixedValue	fixedValue
outlet	inletOutlet	fixedValue	Calculated	inletOutlet	inletOutlet
farfield	Slip	zeroGradient	nutkWallFunction	kqRWallFunction	epsilonWallFunction
blade1	noSlip	zeroGradient	nutkWallFunction	kqRWallFunction	epsilonWallFunction
blade2	noSlip	zeroGradient	nutkWallFunction	kqRWallFunction	epsilonWallFunction
blade3	noSlip	zeroGradient	nutkWallFunction	kqRWallFunction	epsilonWallFunction
blade4	noSlip	zeroGradient	nutkWallFunction	kqRWallFunction	epsilonWallFunction

4.2.5.3. “constant” directory settings:

The settings done in the constant directory settings are of three kinds: defining the boundary conditions types, defining the angular velocity of the propeller(s), and defining the turbulence parameters (k-epsilon model is chosen and dynamic viscosity is set be that of air). Settings for boundary definitions are summarized in the following table for the 0.3 D CRP configuration which contains the largest number of patches:

Table 4-3: Boundary types definitions

Patches	Boundary type	
Inlet	Patch	
Outlet	Patch	
Farfield	Slip	
Blade1	Wall	
Blade2	Wall	
Blade3	Wall	
Blade4	Wall	
Interface_R1-S	cyclicAMI	Neighbouring patch: interface_S-R1
Interface_S-R1	cyclicAMI	Neighbouring patch: interface_R1-S
Interface_R2-S	cyclicAMI	Neighbouring patch: interface_S-R2
Interface_S-R2	cyclicAMI	Neighbouring patch: interface_R2-S
Interface_R1-R2	cyclicAMI	Neighbouring patch: interface_R2-R1
Interface_R2-R1	cyclicAMI	Neighbouring patch: interface_R1-R2

4.2.5.4. 5.2.5.4. "system" directory settings:

The following table summarizes the settings relative to this section:

Table 4-4: Solver settings

ControlDict		
Time Step	Adjustable	
Solver	PimpleFoam	
Functions	Forces	
DecomposeParDict		
Number of processes	4	
Method	Scotch	
fvSchemes		
gradSchemes	leastSquares	
divSchemes	Gauss linear upwind	
laplacianSchemes	Gauss linear limited corrected 0.33	
interpolationSchemes	linear	
snGradSchemes	Gauss linear limited corrected 0.33	
fvSolution		
P	Solver/Smoother	GAMG/ DICGaussSeidel
	Residual	1e-5
Pcorr	Solver/Smoother	GAMG/ DICGaussSeidel
	Residual	1e-2
U; k; eps	Solver/Smoother	smoothSolver/ symGaussSeidel
	Residual	1e-6
Pimple	correctPhi	Yes
	nOuterCorrectors	2
	nCorrectors	2
	nNonOrthogonalCorrectors	1
Relaxation factors	U; k; eps	0.33

It is important to notice that an adjustable time step is used; indeed the solver automatically changes the time step according to the value of the maximal CFL number. Since

the PIMPLE solver and an implicit time scheme are used, the chosen value to impose for the maximal CFL is 25; which yields time steps stabilizing at around 1e-5 s and corresponds to less than 0.035° of the propeller's rotation. Although the maximal chosen value for the CFL is high; it is reached in a very small volume of the computational domain. Figure 4-10 shows only the contours of the CFL number near the isolated propeller at J=0.616; similar results are obtained for all the studied cases. The colour scale is reduced (to between 0 and 5) in order to explicit the problematic zones.

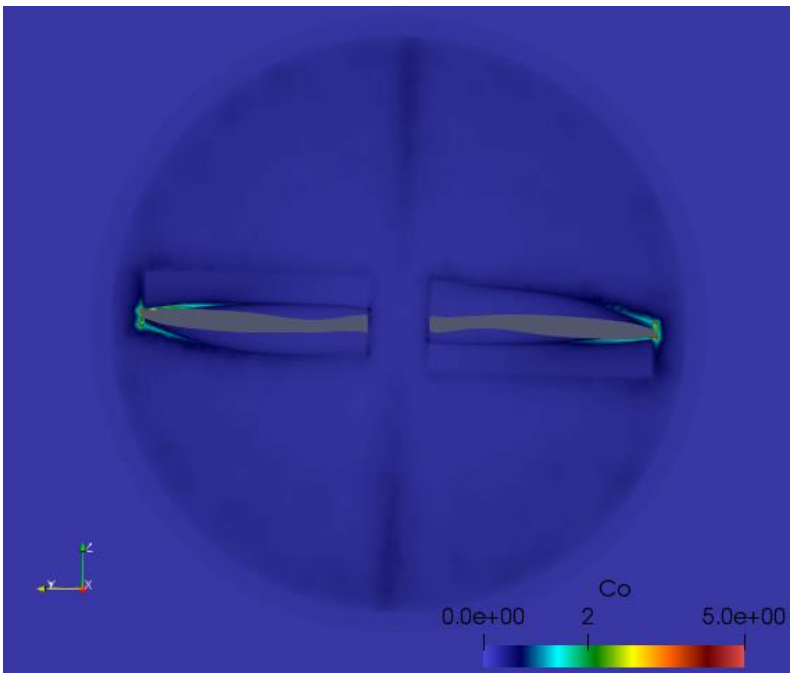

Figure 4-10: Contours of the CFL number near the propeller in the isolated propeller case at J=0.616

4.2.6. Simulation Case Set-Up with ANSYS-Fluent

Fluent is a CFD software included in the ANSYS multi-physics package (version 2023R2 is used), it is a commercial software and offers less control on the case set-up than OpenFOAM, however it has a GUI and is very user-friendly, hence the case set-up with Fluent is a more straightforward (and less time consuming) process.

Only the grid sensitivity analysis is done with Fluent using the MRF technique. The combined use of Fluent and MRF makes the simulation process less time consuming in global, and justifies the use of this approach in the context of having multiple grids to test.

Fluent is selected and an integrated workflow window appears listing the needed steps (geometry, mesh, set-up, solution, results), the grid is directly imported in the mesh section.

Then, in the set-up, the domain is split into two sub-domains (using the "separate" command present in the "zones" section of the "setting up domain" tab) and the correct boundary conditions are inserted (the same as in the OpenFOAM case), interfaces are defined as such and the type of the interface is chosen to be the default. Table 4-5 illustrates the settings of the set-up.

Table 4-5: Case set-up in ANSYS-Fluent

Hypotheses		
Precision	Double precision	
Solver type	Pressure-Based	
Gravity	Neglected	
Velocity formulation	Absolute	
Time	Steady	
Model	Viscous standard k-ε	
Cell zone conditions		
Rotating domain	Frame motion / Relative to cell zone: absolute/Rotation axis: x=1	
Static domain	By default	
Boundary conditions		
Inlet	Velocity Inlet with values of k and epsilon specified as well	
Outlet	Pressure Outlet $P_{out}=P_{in}$	
Wall	Stationary + No Slip	
farfield	Symmetry	
Interface_R-S	Interface	
Interface_S-R	Interface	
Solution Method Configuration		
Pressure-velocity coupling	Coupled	
Gradient	Least Square Cell Based	
Pressure	Second order	
Momentum	Second order upwind	
Turbulent kinetic energy	Second order upwind	
Turbulent dissipation rate	Second order upwind	
Solution Control		
Explicit relaxation factors	Momentum	0.75
	Pressure	0.75
Under-relaxation factors	Density	1
	Body forces	1
	Turbulent kinetic energy	0.8
	Turbulent dissipation rate	0.8
	Turbulent viscosity	1
Miscellaneous		
Residuals	All at 1e-4	
Initialization	Hybrid	
Maximal number of iterations	2000	

The same computational grids used in OpenFOAM are converted into Fluent's ".msh" format.

4.2.7. GRID STATISTICS &GRID SENSITIVITY ANALYSIS

To assess grid sensitivity, four different grids in refinement are tested ranging from 1.1 million cells to 2.5 million cells which are shown in Table 4-6. Grid sensitivity analysis is performed only for the isolated propeller case, with results being transposed to the CRP case. Grid statistics are checked using the command "checkMesh" while located in the case directory.

Table 4-6: Computational grids statistics

		Grid 1	Grid 2	Grid 3	Grid 4
Rotating domain	Number of cells	427,859	471,859	631,735	754,747
	Average orthogonal quality	0.766	0.788	0.799	0.804
	Minimum orthogonal quality	0.153	0.249	0.259	0.229
Static domain	Number of cells	711,880	1,105,850	1,602,250	1,787,250
	Average orthogonal quality	0.990	0.989	0.990	0.990
	Minimum orthogonal quality	0.858	0.825	0.825	0.825
Whole domain	Number of cells	1,139,739	1,577,630	2,233,985	2,541,997
	Average orthogonal quality	0.869	0.895	0.903	0.903
	Minimum orthogonal quality	0.153	0.249	0.259	0.229

The value of thrust is used for grid sensitivity assessment for the advance ratio of J=0.462; the following figure represents the value of thrust on as a function of the total number of elements.

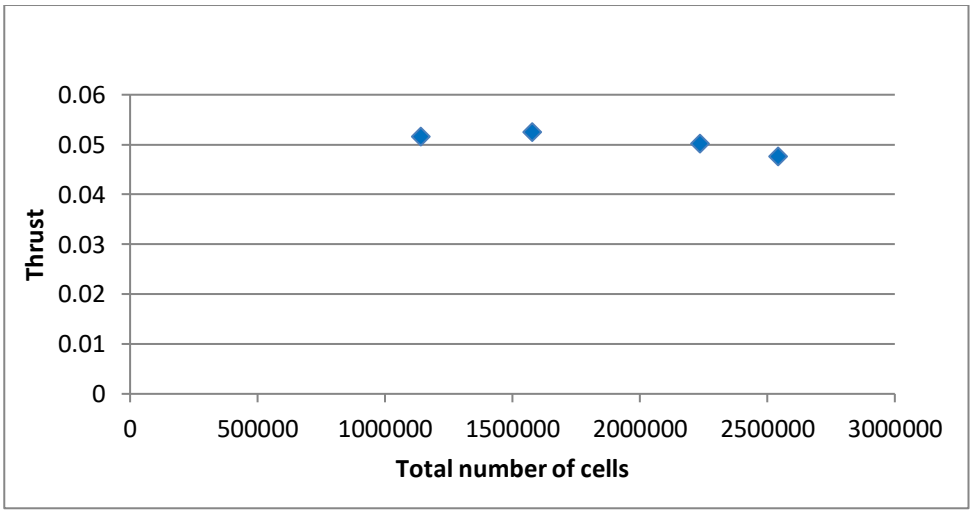

Figure 4-11: Thrust on one blade as a function of the total number of cells

A particularly pertinent consideration to have is computational time since for the CRP configuration, the use of sliding mesh yields better results as the relative positions of the propellers are changing (using MRF, the relative position of propellers stay fixed while the reference frame rotates which is equivalent of adding a rotational speed to the air in the

rotating domain, so changing the phase of the propellers greatly impacts results, specially with a small number of blades like in this case). The disadvantage of this approach lies in its computational cost, hence using MRF to assess grid sensitivity.

As the tested grids yield similar results, the grid containing 1.578 million elements is chosen for all the simulations. This numbers increases with the CRP configurations as indicated by the following table:

Table 4-7: Total number of cells for each tested configuration

Grid	Isolated Propeller	CRP with d=0.3	CRP with d=0.5	CRP with d=1.0
Total number of elements	1,577,630	2,149,410	2,266,730	2,374,592

The value of y+ at the propeller is also verified for each case, the following figures illustrate the values for the isolated propeller scenario at J=0.616; however similar distributions of y+ are obtained in all the studied cases.

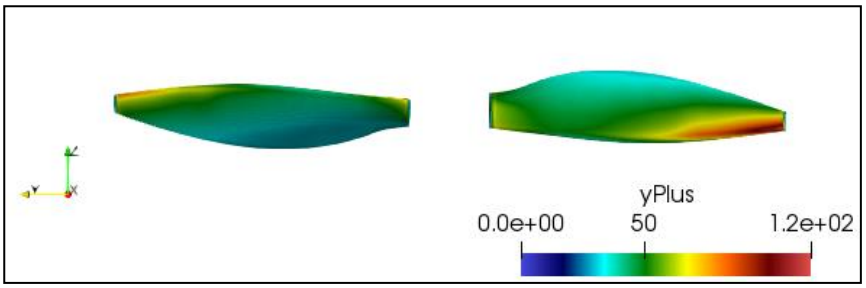

Figure 4-12: Values of y+ at the suction side of the isolated propeller at J=0.616

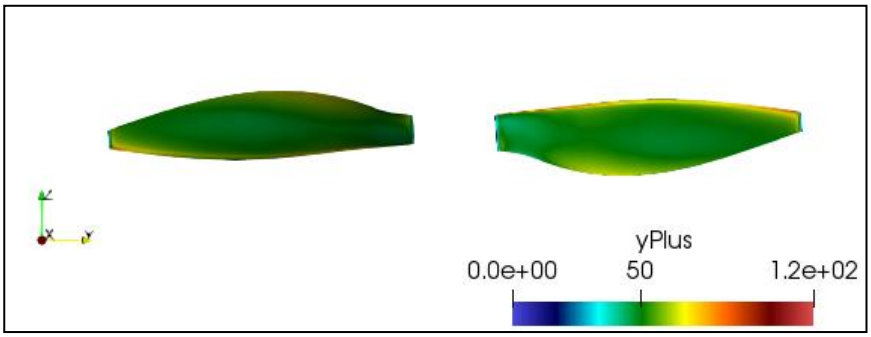

Figure 4-13: Values of y+ at the pressure side of the isolated propeller at J=0.616

4.3. RESULTS

4.3.1. ISOLATED PROPELLER CASE

CFD simulations are performed for different advance ratios with identical parameters as with OpenVSP (with an imposed free stream velocity of 1 m/s). The reason for computing

with a low velocity is to gain computational time; indeed as the rotational speed increases, the CFL number at the tips increases as well, this results in unpractical time steps to cover all the cases within a reasonable amount of time with the available computational resources. Besides, the 1 m/s set of cases is shown to be equivalent to the 3,000 RPM in section 3.3.1.

The observed unsteady behaviour is similar to the one predicted using VLM in the way that all parameters tend to converge toward a stable sustained state, although for the advance ratio of J=0.616, the sustained regime wasn't attained until the fifth revolution. Figure 4-14 shows the variation for the thrust coefficient only, but the same behaviour is observed for the power coefficient and efficiency.

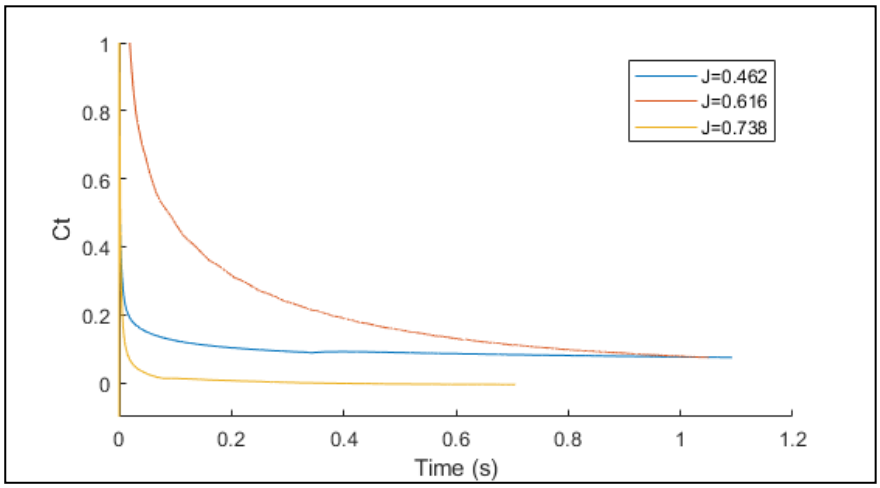

Figure 4-14: Thrust coefficient variation with repsect to time for different advance ratios

In order to conduct the performance study, the average values of the characteristic coefficients over the last revolution of the propeller are taken. Results are then compared to the vortex lattice method and the available experimental data, the thrust and torque coefficients are briefly discussed as the main focus of the study is on efficiency. As the use of k-ε model is known to yield non negligible errors ([7], [16] and [22]), tendency curves are used to perform the analysis.

Figure 4-15 depicts the variation of thrust coefficient with respect to the advance ratio, results from the VLM and CFD approaches are both represented, as well as the experimental data [4] (for the Graupner 10x8 propeller). All the presented data exhibits the same behaviour: the thrust coefficient decreases with the increase of the advance ratio in a quasi-linear manner. However, CFD results differ in the way that the slope of the thrust coefficient is more pronounced; indeed values are over-estimated for low-advance ratios which is consistent with the literature as shown by references [16] and [22] and are under-estimated for high advance

ratios, which can be explained by the energy loss due to recirculation zones causes by the removal of the hub.

Concerning the power coefficient, the same general behaviour as in the work of reference [4] can be observed in Figure 4-16. However, for the same advance ratio, the C_P is over-estimated (at around a double) by CFD. The over-prediction of the C_P is a known consequence of using the k-ε model ([7], [16] and [22]), and is also expected to be amplified by the additional vortices at the blades' roots due to the removal of the hub. It is possible to argue that the VLM gives better predictions of the C_P; however it is preferable to have the C_P over-predicted than under-predicted.

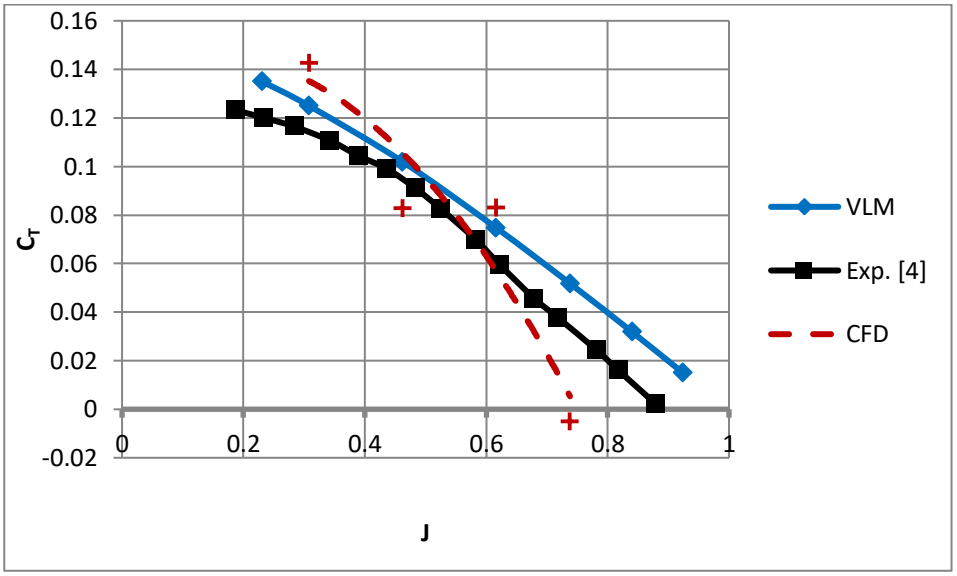

Figure 4-15: Thrust coefficient as a function of the advance ratio for an isolated propeller

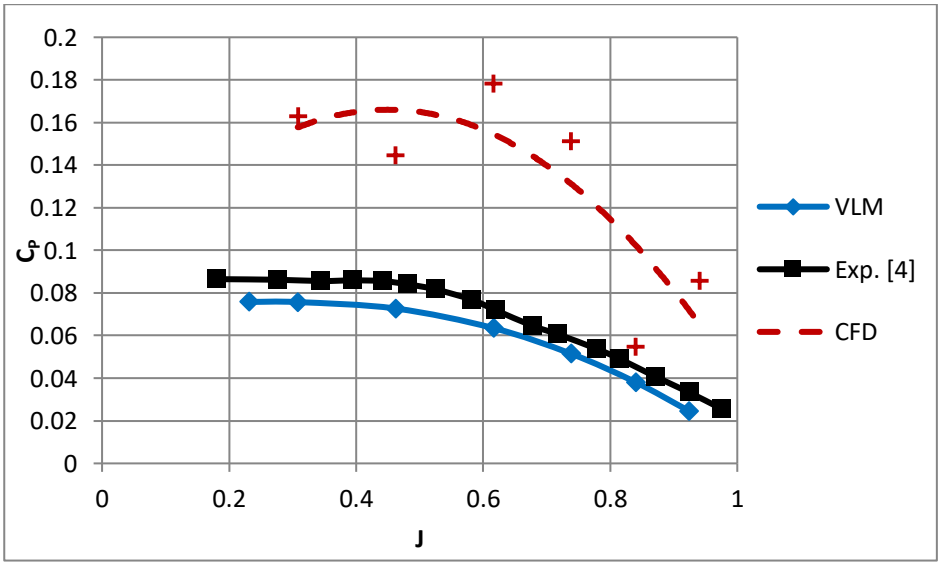

Figure 4-16: Power coefficient as a function of the advance ratio for an isolated propeller

The results of the CFD simulations are most visible in the obtained efficiency shown on Figure 4-17. Indeed, the CFD results, experiments [4] and VLM exhibit the same behaviour; with the efficiency increasing with the advance ratio, reaches a maximum and then decreases. Values obtained through CFD are consistently inferior to the experimental ones, however the under-estimation of efficiency by CFD is known ([7], [16] and [22]) with the effect being accentuated by the removal of the hub (which caused additional vortices, and thus a loss in energy). Although, overall, efficiency is under-predicted; the advance ratio corresponding to the maximal efficiency is close to the one obtained experimentally.

Hence, although the used CFD approach cannot be validated quantitatively, it gives a good qualitative description of the behaviour of efficiency with a good prediction of the position of its maximum value, which corresponds to an advance ratio around J=0.5 (and J=0.55 from reference [4]), a value that the VLM over-predicts by a larger margin.

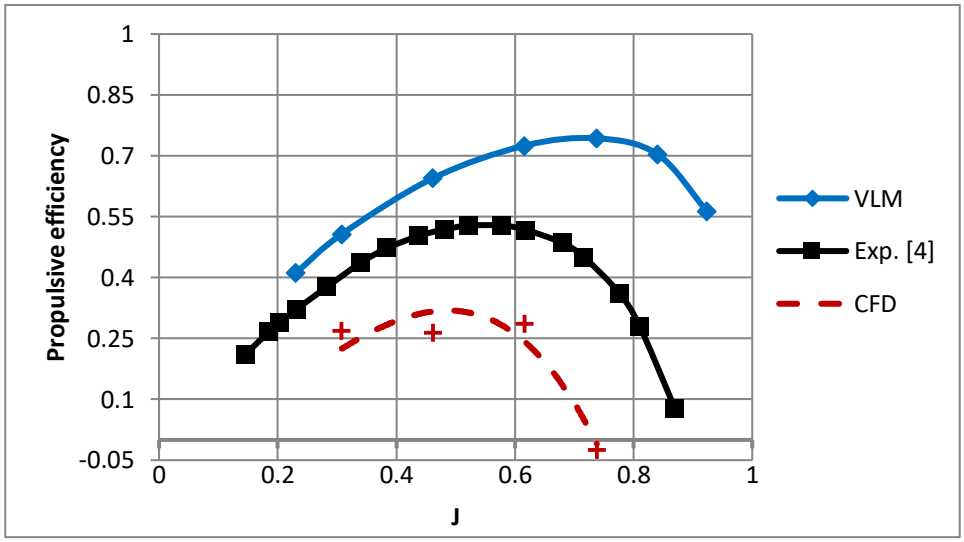

Figure 4-17: Efficiency as function of the advance ratio for an isolated propeller

In order to describe the physical phenomena involved in the isolated propeller case, only the maximal efficiency case is considered in the following figures, at the last time step. The bounds of the colour scale are reduced in order to better visualize the flow structure (with the other cases having similar behaviours of the considered parameters except for J=0.738 which is not the scope of this study as it does not produce thrust).

It is possible to observe on Figure 4-18 and Figure 4-19 that the expected distribution of pressure on the blades is obtained through CFD, indeed the leading edge has an increased pressure (due to the stagnation of the incoming air at the leading edge) but the majority of the suction side is subjected to an under-pressure. On the pressure side of the propeller, the

central area is subjected to an over-pressure with a small under-pressure region near the roots of the blades (caused by the removal of the hub) which can be neglected in practical scenarios.

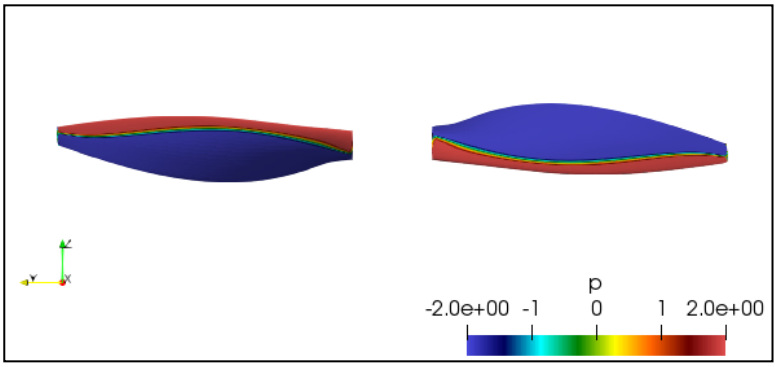

Figure 4-18: Pressure distribution at the front (suction) side of the isolated propeller

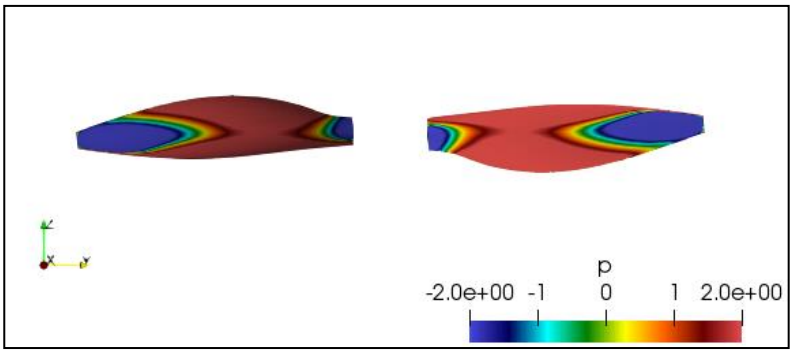

Figure 4-19: Pressure distribution at the back (pressure) side of the isolated propeller

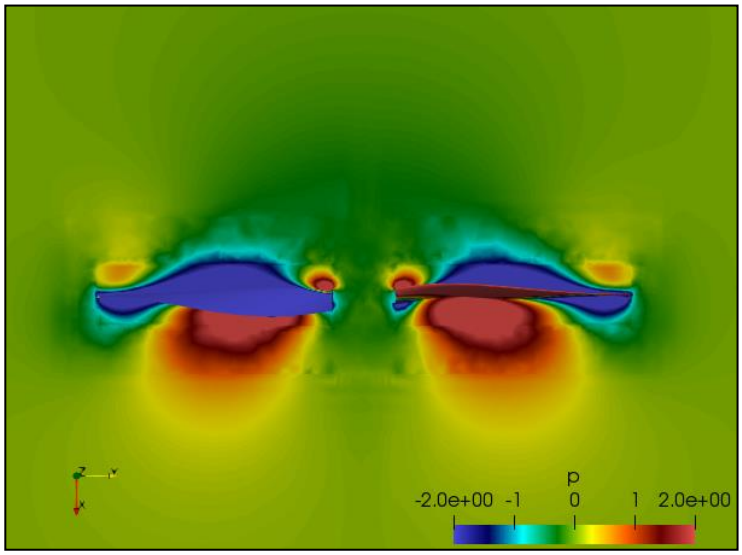

Figure 4-20: Pressure distribution at the slice passing by the centre line of the isolated propeller

However, near the tips of the blades a relatively large under-pressure region which extends to around a quarter of the blade length is observed, the size of the under-pressure region varies with the advance ratio, smaller advance ratios yield a smaller size: the reason being that the relative angle of attack of the propeller blades increases as the advance ratio increases.

It is also important to note that as the inlet velocity is fixed and the reference pressure is zero (which is possible to impose in an incompressible flow), the pressure coefficient is proportional to the pressure distribution, indeed the pressure coefficient can be obtained by multiplying the pressure field by 1.63265.

The pressure field near the propeller is best visualized in Figure 4-20, where a lobe of under-pressure is seen on the suction side of each blade, and a lobe of over-pressure is seen on the pressure side of each blade. Near the root and tips, it is possible to see the over and under-pressure lobes being inverted, which indicates the presence of tip vortices.

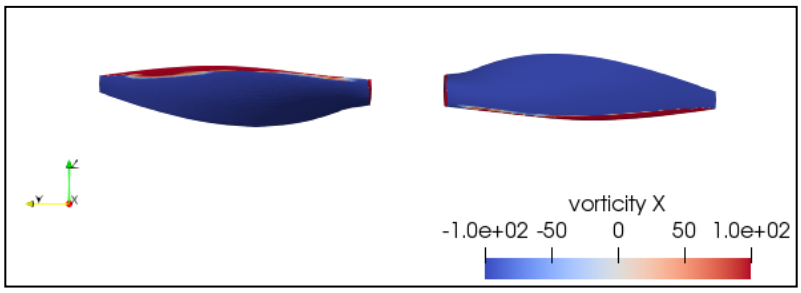

Figure 4-21: Axial vorticity distribution at the front (suction) side of the isolated propeller

It is also possible to notice on Figure 4-21 and Figure 4-22, which represent the distribution of the vorticity in the direction of the propeller's rotation axis that the suction side and pressure side have opposite values of vorticity aside from small pockets on the pressure side. Indeed, the fact that the propeller walls by themselves are regions of high vorticity is to be expected as in all turbo-machinery problems.

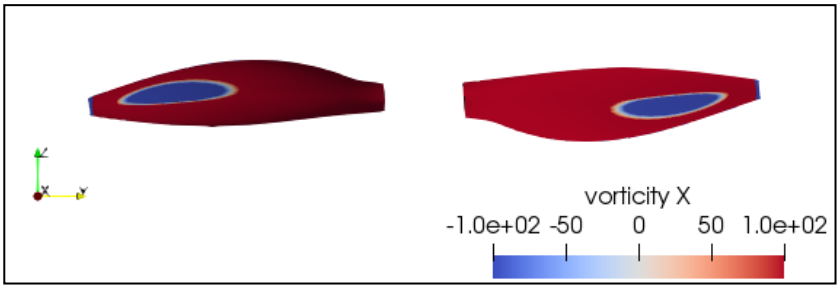

Figure 4-22: Axial vorticity distribution at the back (pressure) side of the isolated propeller

Figure 4-23 shows the vorticity distribution in the region near the propeller (middle plane slice), and indeed it is also possible to observe that the axial vorticity sign does not vary in the vicinity of the blade (unlike what is observed on the propeller walls) with inversions occurring at the tips and roots indicating, again, the presence of tip vortices.

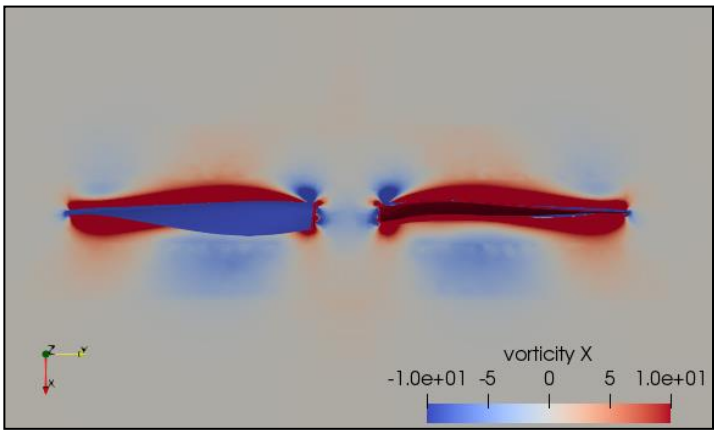

Figure 4-23: Axial vorticity distribution along the slice passing by the centre line of the isolated propeller

Figure 4-24 shows the axial velocity field in the proximity of the propeller, with the positive direction being the free stream direction. It is indeed possible to observe that the air is being pushed stream-wise by the propeller as indicated by the high velocity lobes on the pressure side of the propeller.

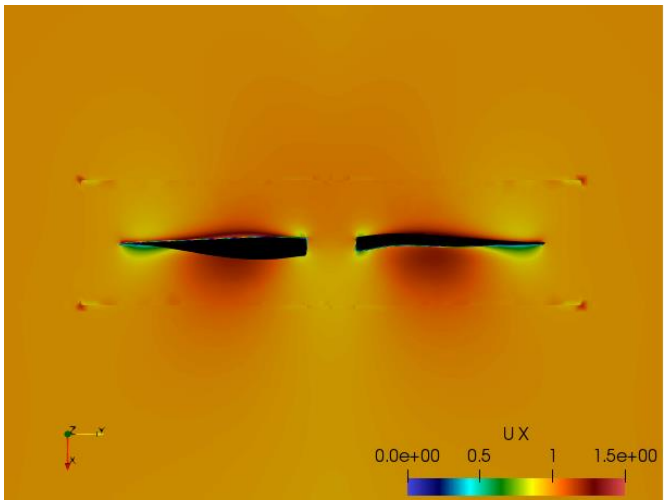

Figure 4-24: Axial velocity distribution along the slice passing by the centre line of the propeller

On the suction side of the propeller, a band of high axial velocity is seen which is due to the airfoil characteristic of the accelerating the flow on its suction side combined with the angle of attack, however this effect is much more pronounced on the peripheral velocity

represented on Figure 4-26. Regions of lower axial velocity are seen near the tips and roots of the blades, further pointing towards the existence of tip vortices.

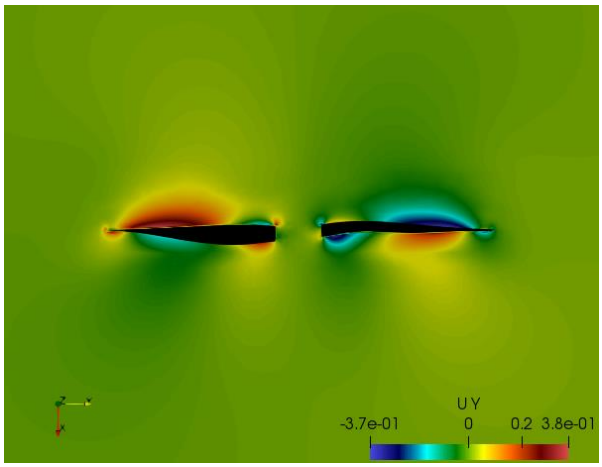

Figure 4-25: Radial velocity distribution along the slice passing by the centre line of the isolated propeller

In addition to the clues in the pressure and axial velocity fields indicating the presence of tip vortices, the change in velocity from centrifugal to centripetal is best described by Figure 4-25 representing the radial velocity field at the middle plane. Indeed, an anti-symmetrical field between the suction and pressure side is observed, with air from the pressure side moving toward the tips, and air from the suction side moving toward the roots (if the opposite behaviour near the tips caused by the hub's removal is neglected). At the very tips the opposite behaviour is seen.

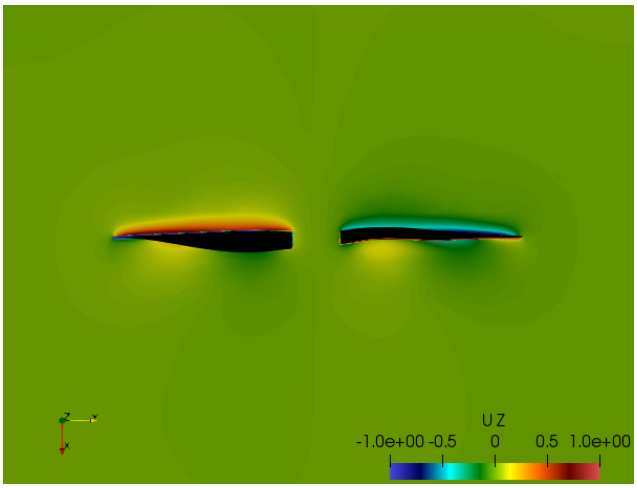

Figure 4-26: Peripheral velocity at the slice passing by the centre line of the isolated propeller

Therefore, it is possible to assume that tip vortices are generated in this case, with velocities having been also highly impacted by the removal of the hub. It is also possible to

argue from the previous observations that the removal of the hub is a major cause of the significant loss in efficiency.

The only observation that can be made from Figure 4-26 is that an increased velocity is found on the suction side of the propeller and that the velocity decreases in the pressure side which is in line with the normal behaviours of an airfoil.

In order to visualize the wake development, contours of vorticity are shown for different planes normal to the stream direction at distances of 0.1D, 0.25D and 0.5D on Figure 4-27, the same scale from -1 to 1 is used in order to assess the change in intensity in addition to structures.

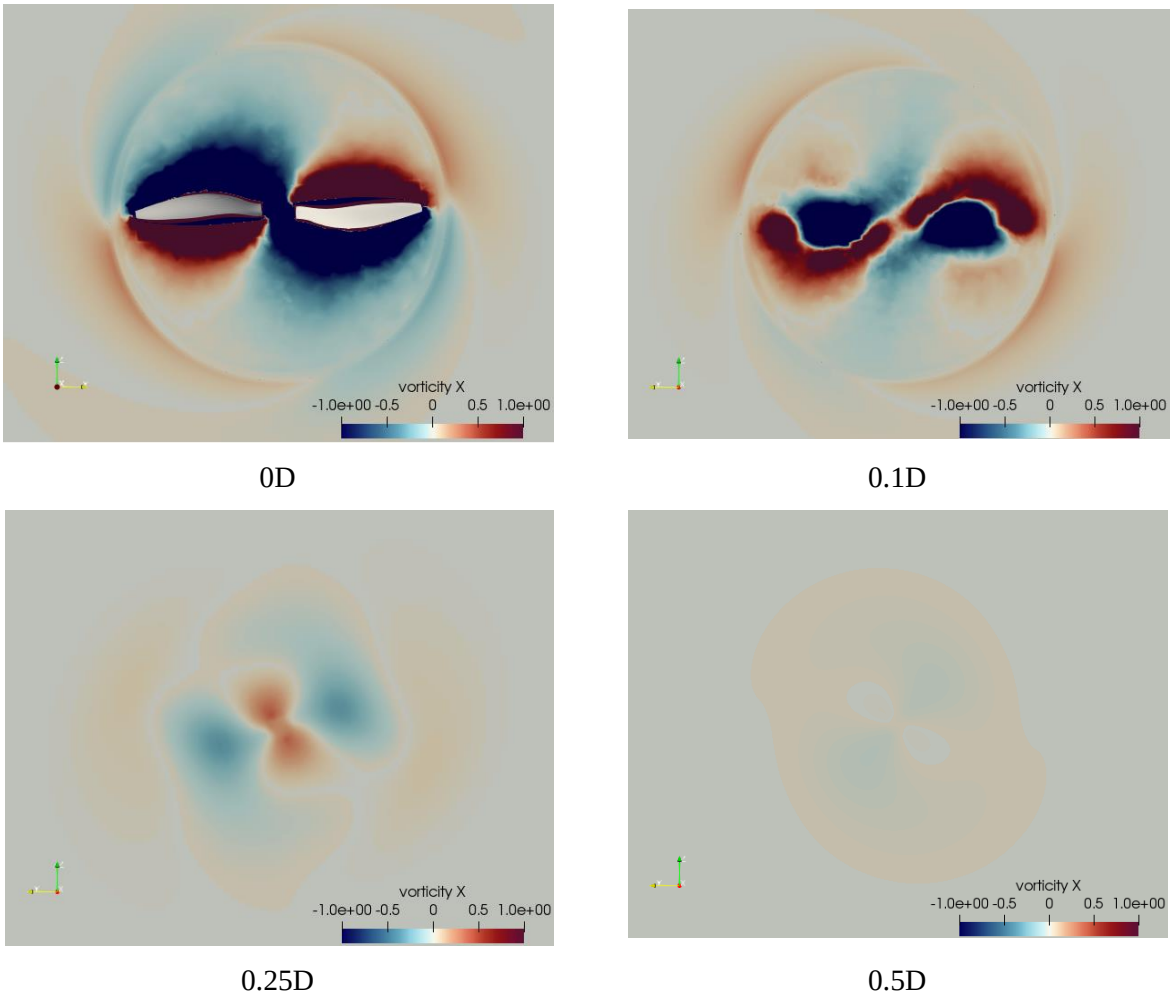

0D 0.1D

0.25D 0.5D

Figure 4-27 : Vorticity distribution at the wake of an isolated propeller at J=0.616

The first observation to be made is that the vorticity field (which is indicative of the generated turbulence) tends toward a uniform zero state at a short distance from the propeller, indeed at the distance of 0.5D the field is barely perceptible, and this can be attributed to the high advance ratio and/or the shortcomings of the k-ε model.

Coherent structures can be observed which is indicative of the presence of vortices, with the removal of the hub having a significant effect. Indeed, at the proximity of the propeller (positions 0D and 0.1D), the structures follow the shape of the blades: a lobe having an "s" shape and two opposite lobes enveloped by the previous one. However, at distances of 0.25D and 0.5D, the "s" shaped structure separates into two distinct lobes normal to the opposite ones making a clover-shaped pattern which intensity decreases with distance. In the considered CRP cases, the aft propeller is placed at distances where the clover pattern is observed.

To conclude on the isolated propeller case, CFD simulations using the k-ε model yield good qualitative results with a correct phenomenological description of the pressure, vorticity and velocity fields aside from abnormalities which are purely due to the removal of the hub, and from a quantitative point of view, results need true experimental verification to be assessed, although the deviation from experimental data is expect to be significant. However, as the simulations do predict the main flow structures and physical phenomena, this framework is suitable to estimate the general behaviour of propellers at a lower computational cost than more intrinsically accurate models, which justifies its use in the CRP cases.

4.3.2. CONTRA-ROTATING PROPELLERS CASES

Simulations are performed for three CRP cases characterized by their inter-propeller distance d. The chosen distances are d=0.3D, d=0.5D and d=1.0D. Only the advance ratio which yielded the maximum efficiency in the isolated propeller case is considered (J=0.616), although results are expected to differ with the advance ratios (as shown by the VLM simulations).

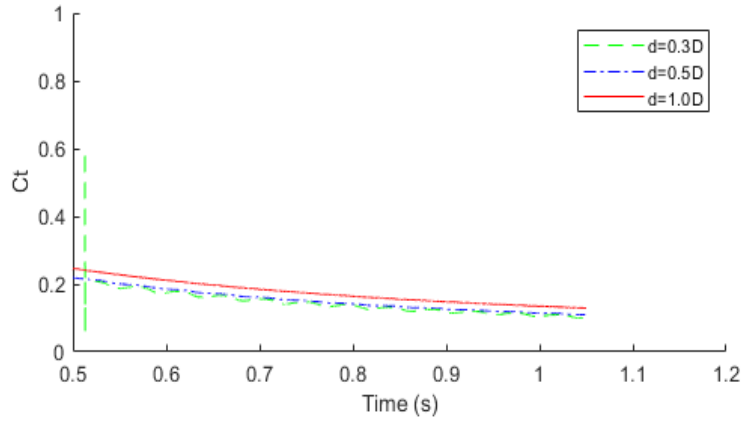

Figure 4-28: Thrust coefficient variation over time for different CRP configurations

The observed unsteady behaviour is similar to the one predicted by OpenVSP, the sustained regime is considered to be achieved at the fifth revolution (around 0.95s) because of the slow convergence towards this sustained regime. Figure 4-28 shows only the variation of the thrust coefficient, but the power coefficient and efficiency exhibit the same behaviour (the irregularity seen in the curve representing the distance d=0.3D is solely due to simulation being paused and resumed).

As with the VLM approach, oscillations of the thrust coefficient (the torque coefficient exhibits an identical behaviour), as well as efficiency are observed and are shown in the figures below.

Firstly, it is observable that the oscillations of the thrust coefficient and efficiency are of lower amplitudes than the ones predicted by VLM. Also, the amplitude decrease with respect to distance is much more pronounced than what is predicted by the VLM; indeed oscillations are barely distinguishable at d=0.5D and absent at d=1.0D.

Secondly, it is also important to note that the frequency of the oscillations is identical to the one predicted by VLM: namely, four times the propeller rotational frequency ($\varphi = 4 \times N$) and that the oscillations' amplitudes of the fwd and aft propeller are nearly equal (which was not the case in the VLM approach). Hence, the Strouhal number is still equal to 0.142 which justifies the use of average values for the performance study.

Another observation is that the thrust coefficient and efficiency of the aft propeller are distinctively higher than those of the fwd propeller, which is expected to happen since the aft propeller has an advantageous incoming swirling flow caused by the fwd propeller (this behaviour was not predicted by the VLM). The difference between the fwd and aft propellers is best seen on the efficiency plots (Figure 4-32 to Figure 4-34). The difference in efficiency is around 0.02 for distances of d=0.3D and d=0.5D; however it is negligible for d=1.0D meaning that that the fwd propeller wake has little to no effect on the performances of the aft propeller.

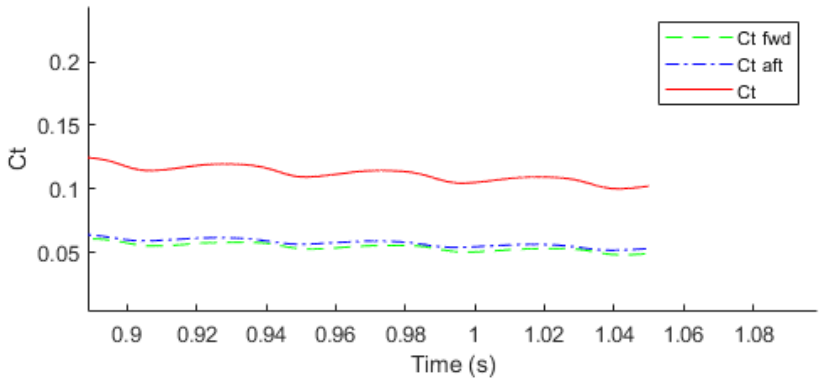

Figure 4-29: Thrust coefficient variation with respect to time for a spacing of d=0.3D

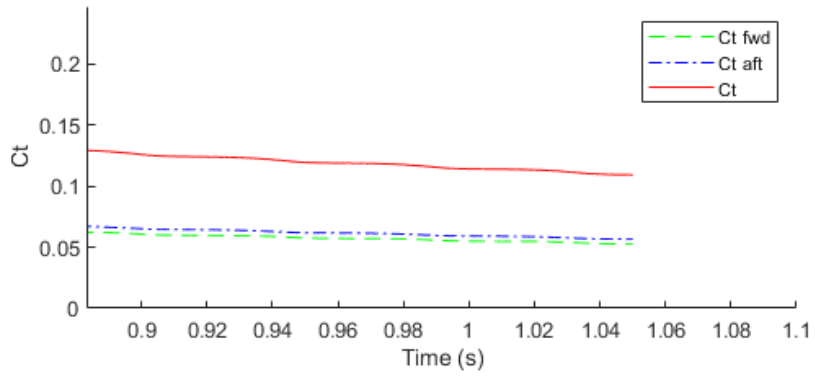

Figure 4-30: Thrust coefficient variation with respect to time for a spacing of d=0.5D

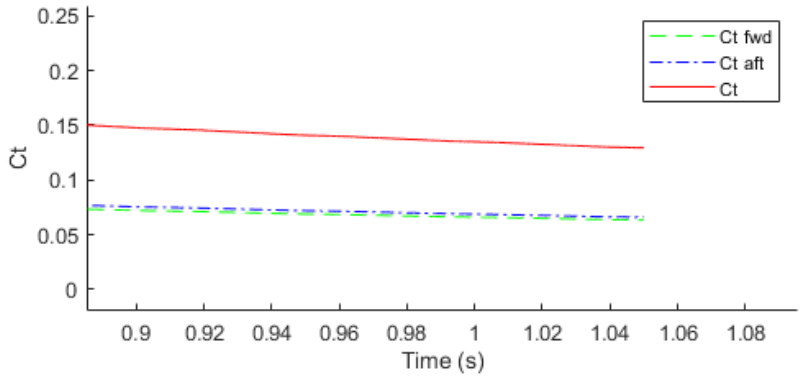

Figure 4-31: Thrust coefficient variation with respect to time for a spacing of d=1.0D

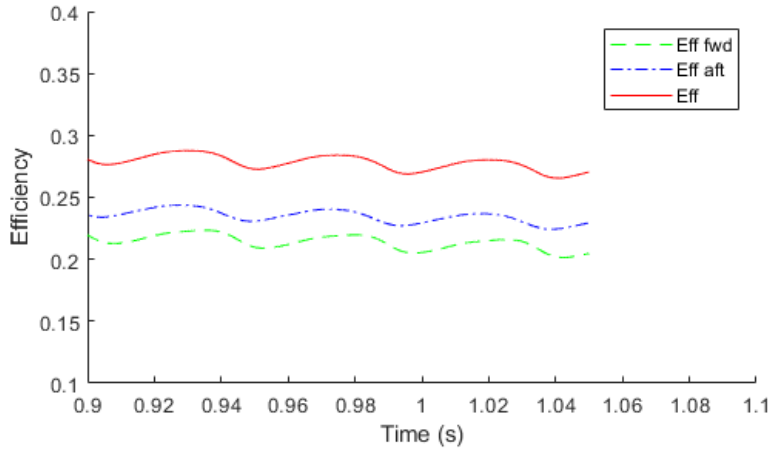

Figure 4-32: Efficiency variation with respect to time for a spacing of d=0.3D

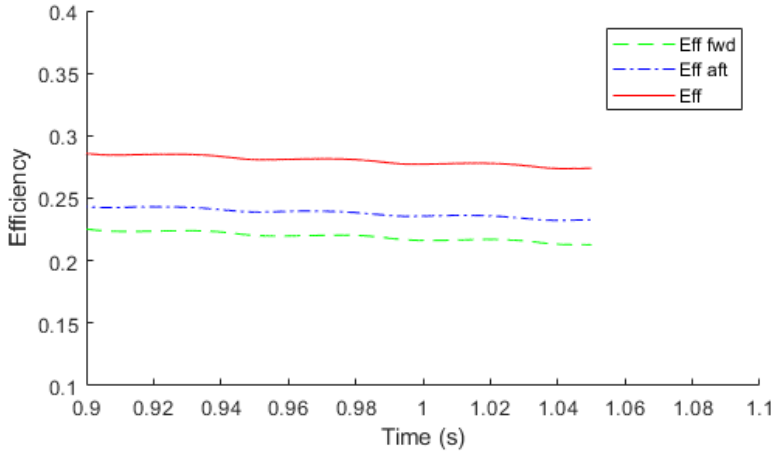

Figure 4-33: Efficiency variation with respect to time for a spacing of d=0.5D

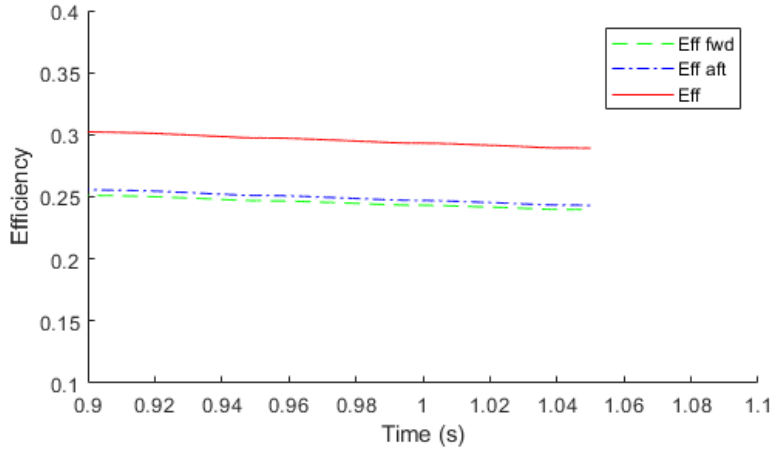

Figure 4-34: Efficiency variation with respect to time for a spacing of 1.0D

In order to assess the influence of spacing on performance, the average parameters of the last revolution are considered, yielding the following results:

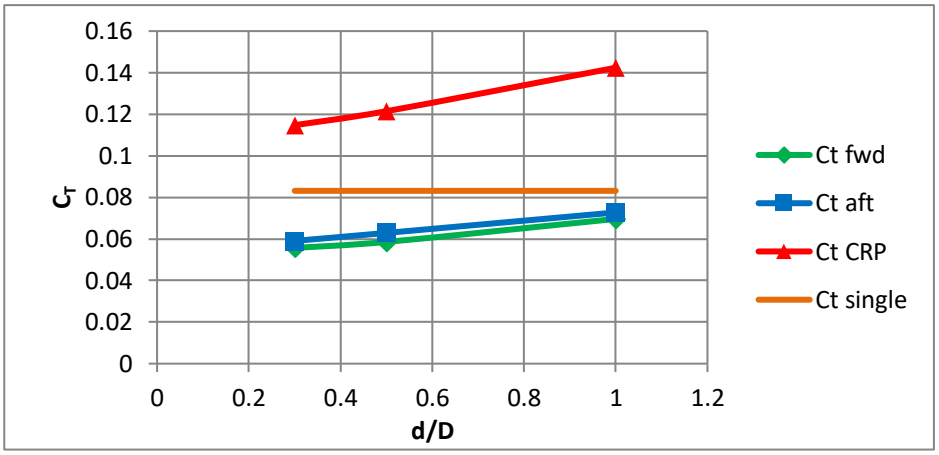

Figure 4-35: Thrust coefficient with respect to dimensionless inter-propellers distance at J=0.616

Indeed, it can be seen on Figure 4-35 and Figure 4-36 that the thrust and torque coefficients increase significantly with the increase of spacing (from a spacing of d=0.3D to d=1.0D, the C_t increased by 24 % and the C_p by 14 %). The variation law of the C_T and C_P seems linear in the considered region, but the coefficients are expected to stagnate starting from the point where the wake of the fwd propeller does not influence the performance of the second propeller (meaning, d>1.0D).

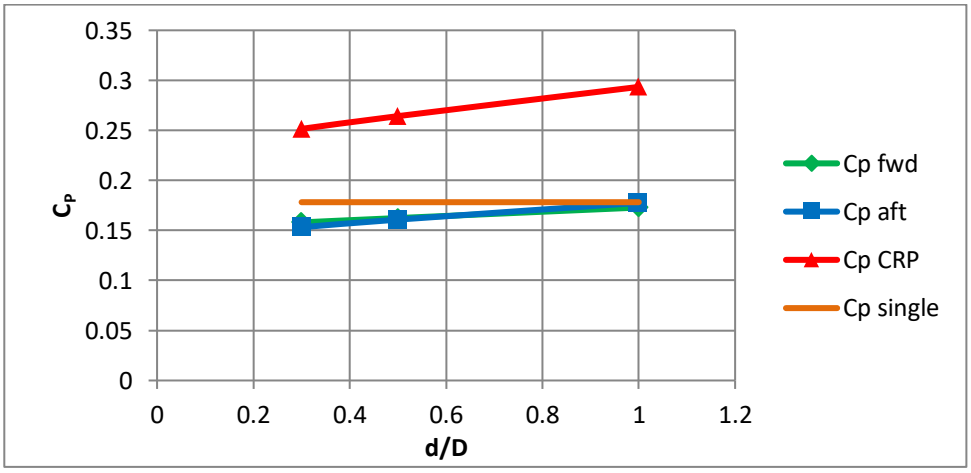

Figure 4-36: Power coefficient with respect to dimensionless inter-propellers distance at J=0.616

Other observations to be made are:

- That the $C_T$of the fwd and aft propellers, if considered individually, are inferior to the C_T of the isolated propeller case although combined give a much higher value;

- That the C_P of the fwd and aft propellers, if considered individually, are inferior to the C_P of the isolated propeller for small spacing, and converge toward the latter as the spacing increases. If combined, the resulting C_P is higher than the one of the single propeller case.

These results are expected and can be attributed, on the one hand to the fact that the torque of each propeller is countered by the torque of the other, thus reducing the required power to rotate each propeller with the effect being more pronounced for shorter inter-propeller distances; on the other hand the decrease of the thrust coefficient can be attributed to the fact that the flow in the vicinity of the propeller is simply more turbulent as the spacing decreases.

Concerning efficiency (Figure 4-37), although the individual efficiencies of the fwd and aft propeller are lower than the efficiency of an isolated propeller, the efficiency of the whole CRP system is almost identical, with it being slightly inferior for spacings of 0.3D and 0.5D, and slightly superior for the 1.0D spacing. Indeed, the results obtained through CFD are very different to ones predicted by VLM: relative to the isolated propeller case (and for the same advance ratio), the efficiency of the CRP predicted by VLM is inferior with a difference of around 0.03, whereas CFD predicts the same efficiency (slight variations). It is also important to note that the efficiency increases with the spacing (an increase of 6.3%: however this value is not valid in practical scenarios since the efficiency is known to be under-estimated making the relative increase higher).

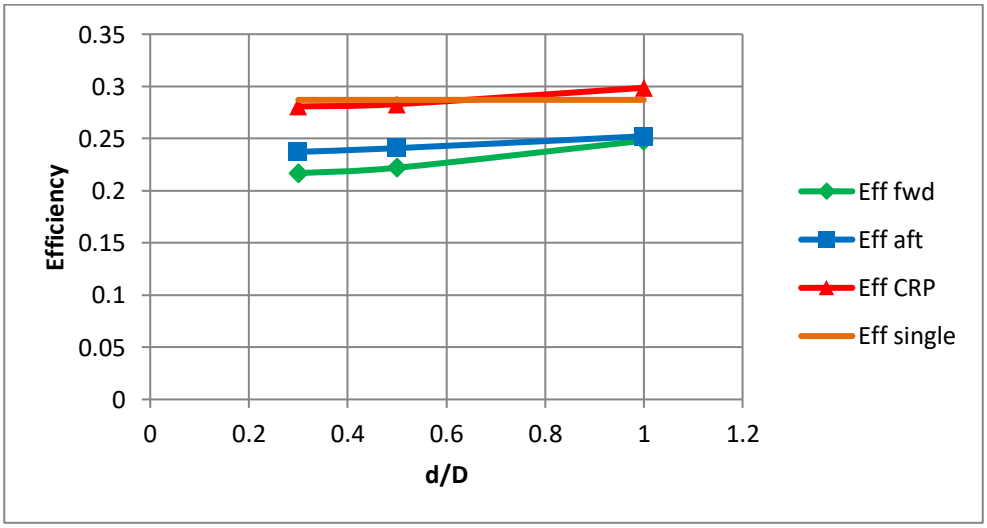

Figure 4-37: Efficiency with respect to dimensionless inter-propeller distance at J=0.616

Another observation that stems from these results, is that CRPs produce more thrust than an isolated propeller with the same efficiency making CRPs advantageous in terms of performance.

Finally, it is important to remind that these results are only valid for the considered advance ratio, and in order to gain a complete description, simulations must be performed for other advance ratios which would require increased computational time and resources. However, since the effect of the advance ratio on efficiency is more pronounced than the effect of spacing, performing simulations for the maximal efficiency advance ratio can be justified for practical applications.

For the qualitative description of the physical phenomena present in CRP systems, only the case where the propeller blades are not aligned is considered; the reason being that when the propellers are perfectly aligned, the pressure, velocity and vorticity fields are near identical to the ones expected from two isolated propellers, and that the interaction between the two propellers is not seen clearly.

Figure 4-38 shows the pressure field near each of the fwd and aft propellers for all the studied CRP configurations, slices are taken in fwd and aft propellers planes. It can be seen that the pressure fields near the propellers are almost identical for all cases, however differences is the inter-propeller region can be noted.

For a spacing of d=0.3D: the over-pressure lobes on the pressure side of the fwd propeller extend further downstream and are directed slightly at the rotation axis. They create an over-pressure region to which the aft propeller is subjected to, which can explain why the aft propeller outperforms the fwd in terms of efficiency. It can be also seen that the under-pressure region induced by aft propeller is smaller than the one of the fwd propeller, which can explain that even if the aft propeller is more efficient than the fwd one, the performances of the individual propellers in a CRP system are inferior to the isolated propeller;

For a spacing of d=0.5D: the over-pressure lobes do not extend to the aft propeller, however the under-pressure region induced by the aft propeller does. However the under-pressure intensity is still lower than the one of the fwd propeller. The larger under-pressure region combined with the absence of the influence of the over-pressure lobes cause by the fwd propeller can explain why the aft propeller performs better than the fwd one.

As for a spacing of d=1.0D, no visible interaction between the propellers can be seen in the pressure fields

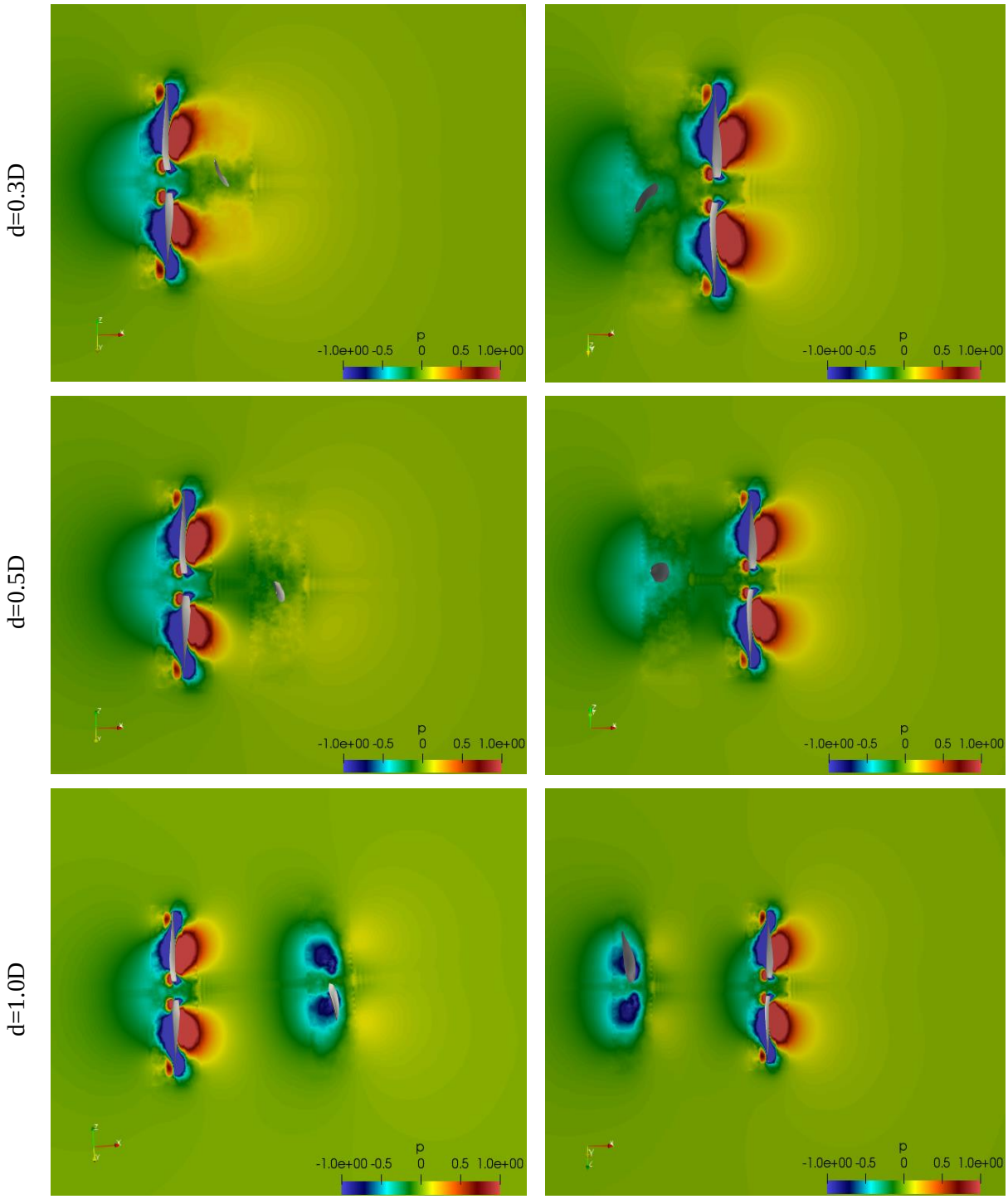

Figure 4-38: Pressure field for fwd and aft propellers for different CRP configurations

Concerning the velocity fields (shown in Figure 4-39), no visible interaction can be observed with the velocity fields near the propellers, being near-identical to the one observed in the isolated propeller case.

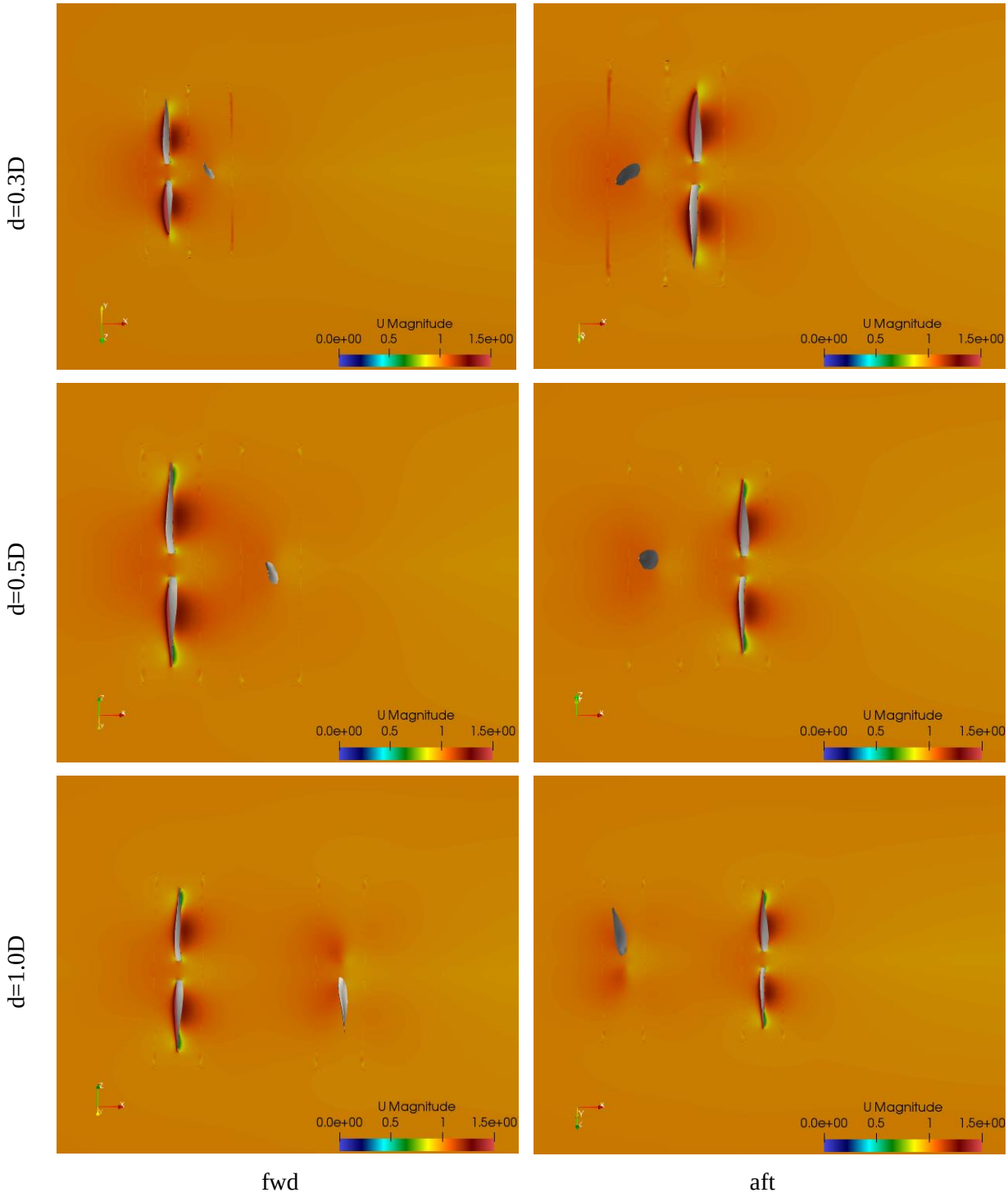

Figure 4-39: Velocity field near the fwd and aft propellers for different CRP configurations

Figure 4-40 to Figure 4-43 show the vorticity distribution (in the direction of the propeller rotation) in the region between the two propellers in the CRP cases; the vorticity

field is sliced at equal percentages of the inter-propeller distance (and not the distance from the fwd propeller) in order to compare the studied cases. The same scale of vorticity is kept in order to compare vortical structures as well as their intensity; all the slices have been oriented to have a front view (x axis pointing inwards) meaning that positive values are in the direction of the fwd propeller rotation (clockwise).

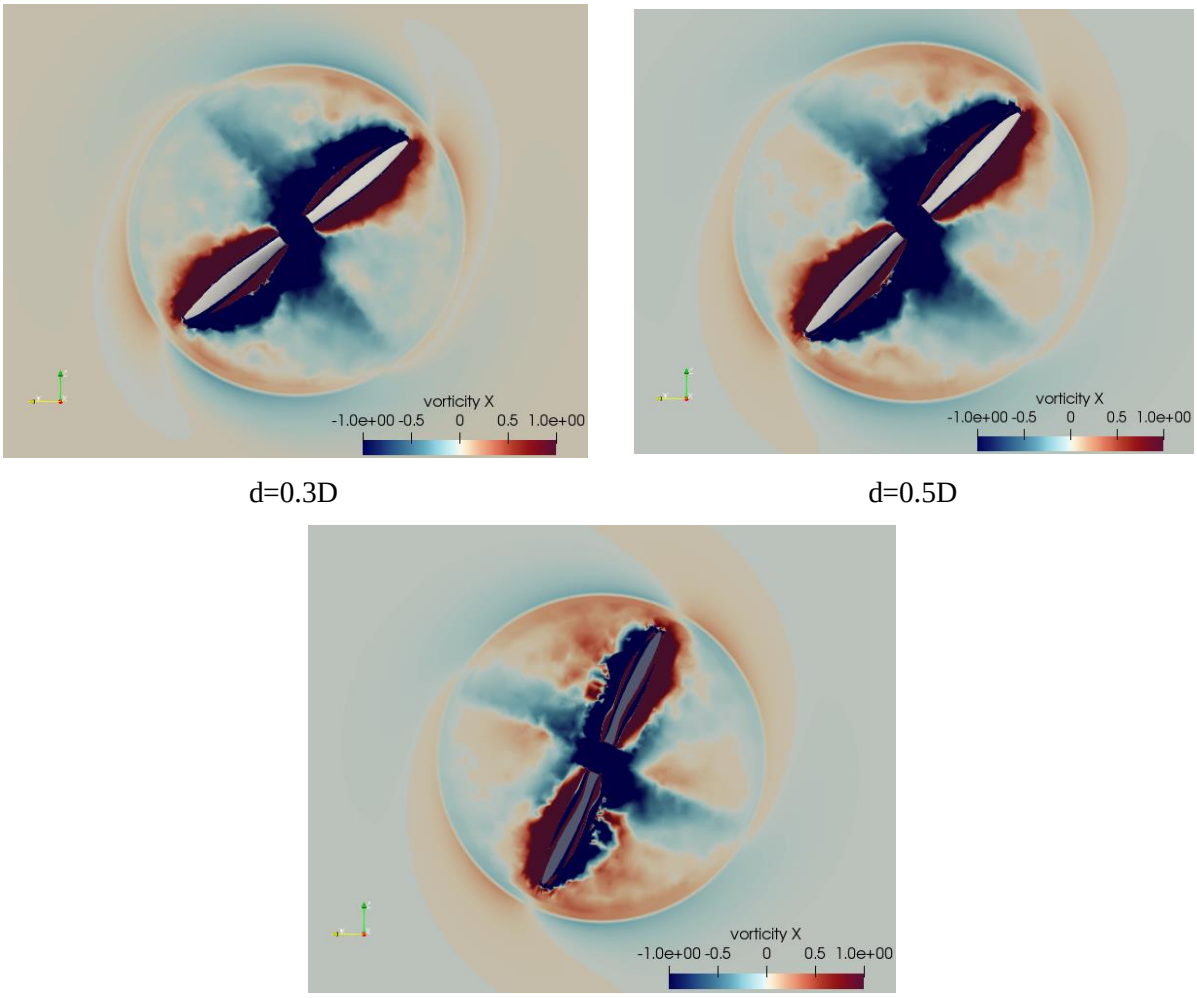

d=0.3D d=0.5D

d=1.0D

Figure 4-40: Vorticity field at the fwd propeller (distance of 0d) for different CRP configurations

It can be seen from Figure 4-40 that for inter-propeller distances of 0.3D and 0.5D, the vorticity distribution at the fwd propeller is very similar to the one of an isolated propeller; however for a spacing of 1.0D, the distribution is perturbed and structures are thinner although conserving the main features (an “s” shaped zone enveloping two inverted vorticity lobes).

Figure 4-41 shows the vorticity distribution at 25% of the inter-propeller distance, again spacings of d=0.3D and d=0.5D exhibit the same structures but the ones corresponding to the

larger spacing having an inferior intensity. This is solely due to the increase in spacing. However, in the CRP case having a spacing of d=1.0D different structures are predicted; indeed the predicted structures are very similar to the ones predicted for the isolated propeller wake at the same distance (namely 0.25D).

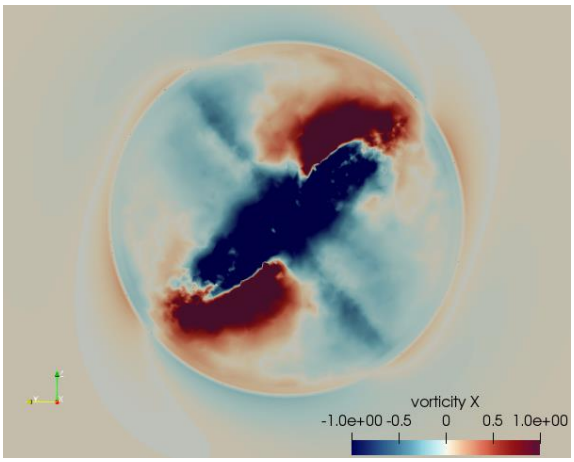

d=0.3D

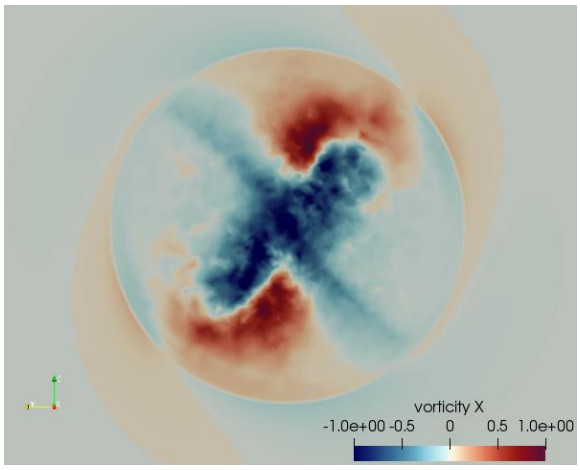

d=0.5D

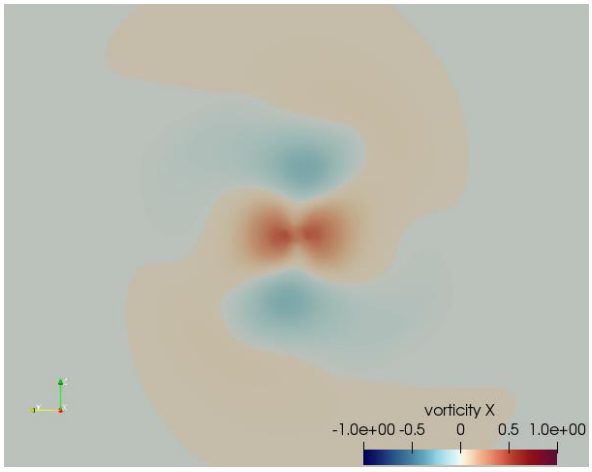

d=1.0D

Figure 4-41: Vorticity field at a downstream distance of 0.25d from the fwd propeller for different CRP configurations

Figure 4-42 shows the vorticity distribution for the plane halfway between the two propellers; in this case very different structures are predicted for each spacing:

- For d=0.3D: two positive vorticity lobes which are separated by a negative vorticity linear region, there is an overall equilibrium where neither positive nor negative regions dominate the flow;
- For d=0.5D: the clover pattern seen on the isolated propeller wake for a similar distance (0.25D) is seen, however the intensity is of the lobes is higher and the

vicinity of the clover pattern has a positive vorticity indicative of the still present influence of the fwd propeller;

- For d=1.0D: vortical structures are not visible (in the [-1;1] scale), however, vorticity has a positive value on the ring in which the blade tips are located.

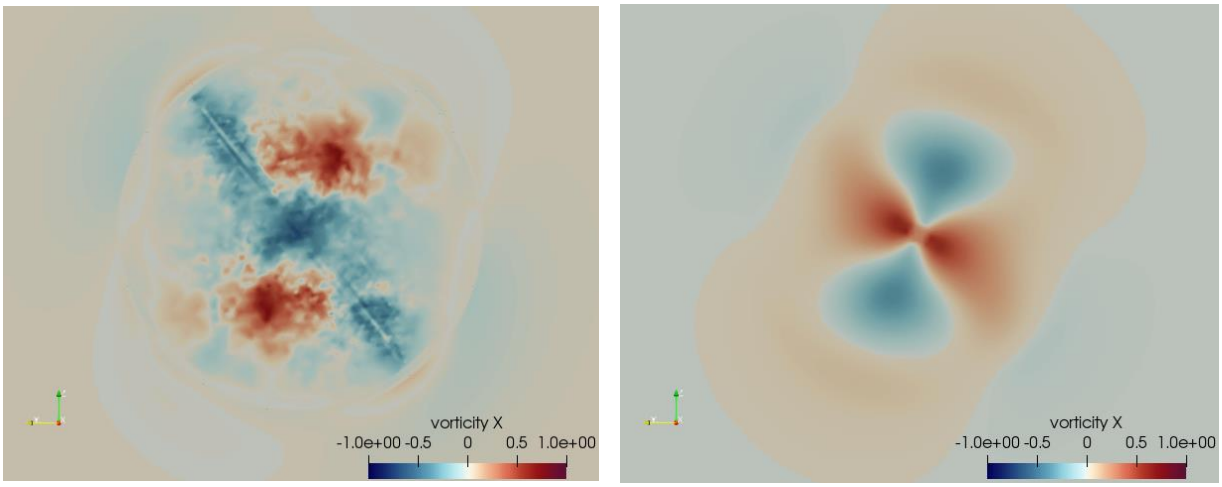

d=0.3D d=0.5D

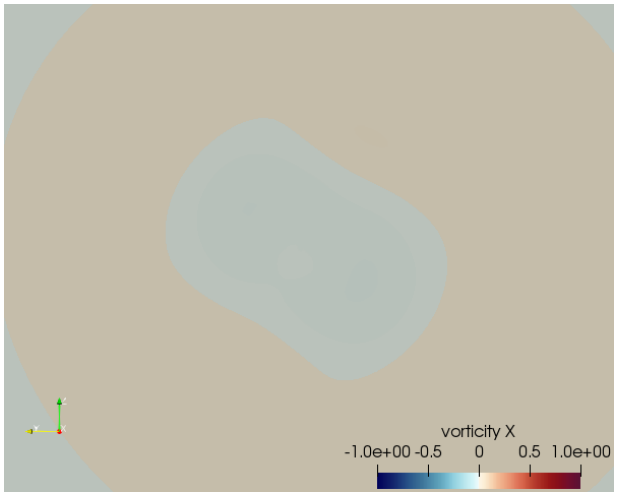

d=1.0D

Figure 4-42: Vorticity field at a downstream distance of 0.5d from the fwd propeller for different CRP configurations

The influence of both propellers on the vorticity field is best seen on Figure 4-43 which represent a slice at 75% of the inter-propeller distance; it is possible to observe for the configurations of d=0.3D and d=0.5D that the vortical structures can be described as a superposition of the fwd propeller induced structures and the aft propeller induced structures, indeed the clover pattern is superimposed to the "s" pattern in those cases. For the d=1.0D case, there is no superposition, the vorticity is characteristic of the aft propeller only, however

the slightly positive vorticity in most of the field near the propeller indicates that the swirl due to the fwd propeller is still present.

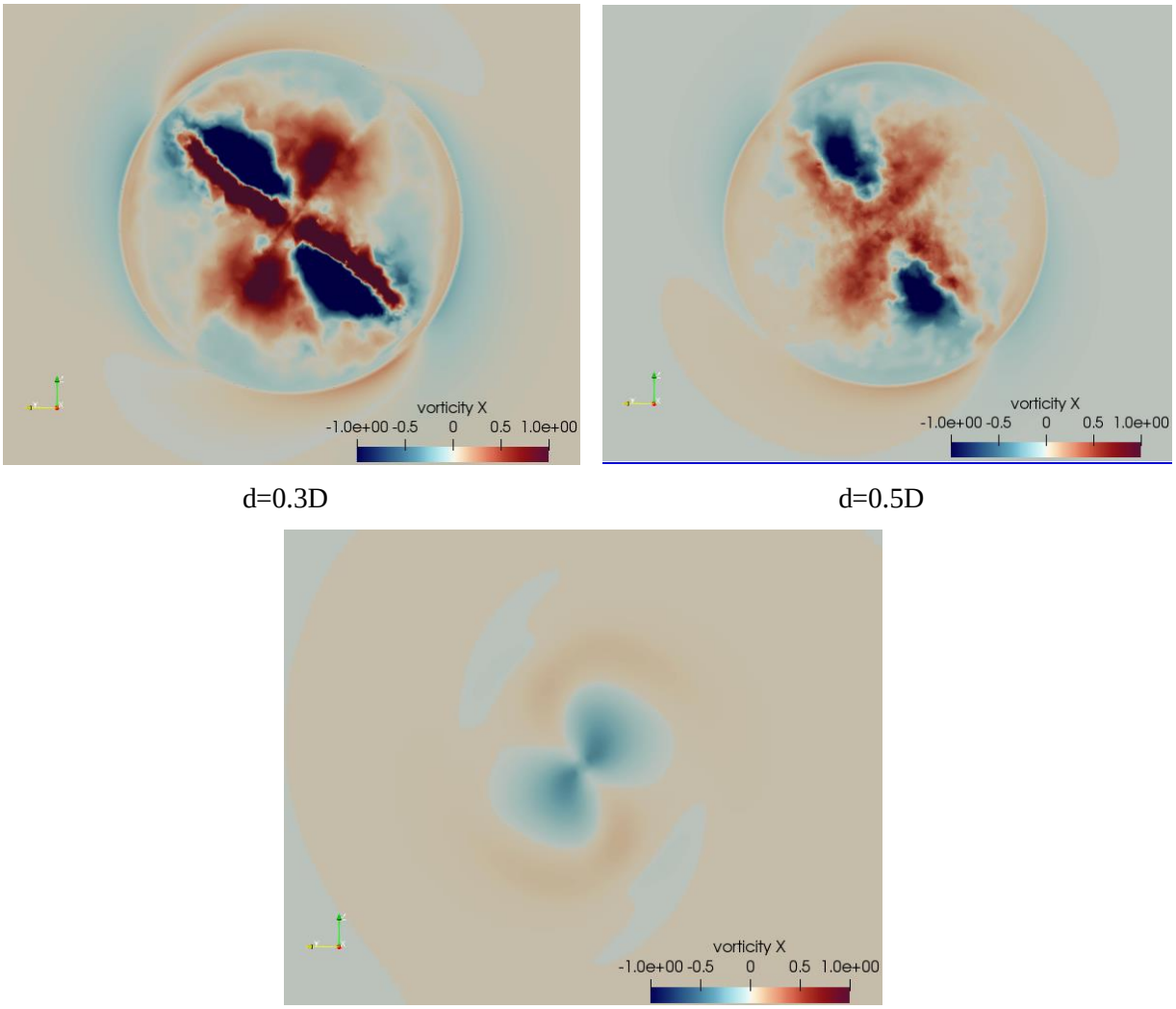

d=0.3D d=0.5D

d=1.0D

Figure 4-43: Vorticity field at a downstream distance of 0.75d from the fwd propeller for different CRP configurations

Figure 4-44 and Figure 4-45 show the vorticity distribution in the wake of the isolated and aft propeller of the considered CRP configurations. Unlike in the assessment of the vorticity field in the inter-propeller region, the slices are taken at distances referenced by the diameter (0.1D and 0.25D), meaning that the distance is equal in the four shown configurations.

In Figure 4-44, it is possible to compare the wakes of the CRP configurations to the isolated propeller case for a distance of 0.1D. Similar structures are predicted for spacings of 0.3D and 0.5D with a positive vorticity “x” shaped structure, which is a superposition of two linear structures generated by the fwd and aft propellers (with the thicker line being generated

by the aft propeller), two negative vorticity lobes are also predicted at the extremity of the thick positive line. For the d=1.0D CRP case, the positive structure is reduced in size with the legs of the "x" barely visible, the negative vorticity lobes are larger and envelop the positive vorticity region (with small spots of positive vorticity).

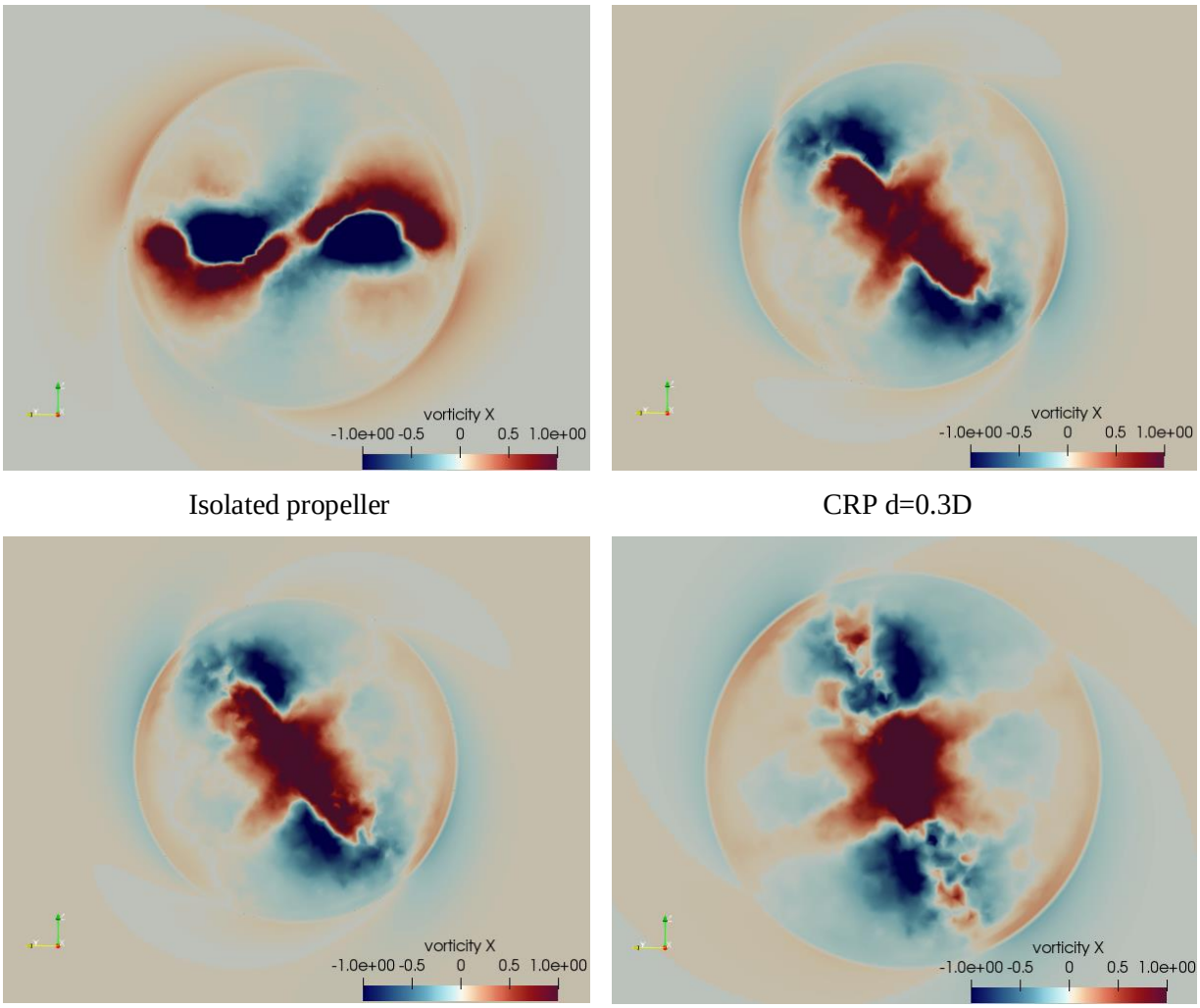

Isolated propeller CRP d=0.3D

CRP d=0.5D CRP d=1.0D

Figure 4-44: Vorticity field at a downstream distance of 0.1D from the aft propeller for all studied cases

Figure 4-45 show the vorticity field at a distance of 0.25D, it is clear that the decrease of vorticity in magnitude is similar to the one of an isolated propeller; the predicted vortical structures are also almost identical to the isolated propeller case (but in reverse as the rotation directions are opposite); this can be attributed to the prediction that the wake generated by the fwd propeller has lost all of its perceptible intensity at this distance and only the effect of the aft propeller is present at this distance.

Results, although qualitative, predict an efficiency increase with the increase of spacing. The reason, as expressed by the slices of the vorticity field, is the dissipation of the turbulence in the wake of the fwd propeller while the flow swirl induced by it, is preserved.

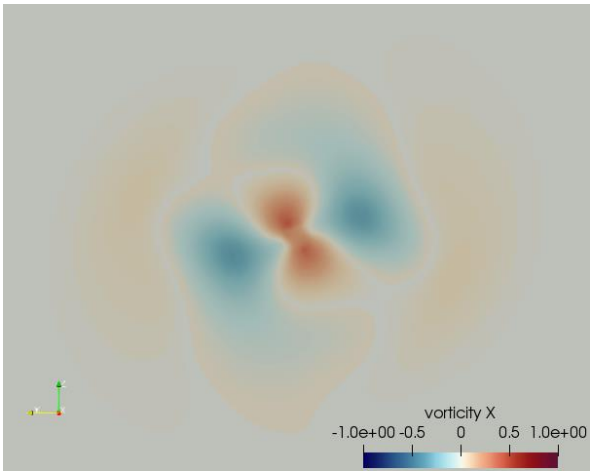

Isolated propeller

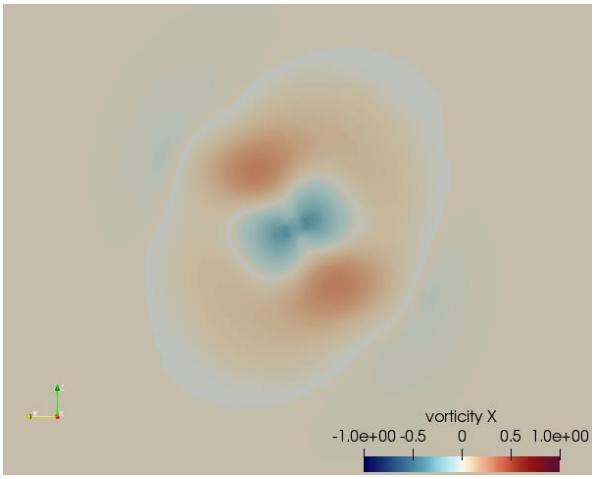

CRP d=0.3D

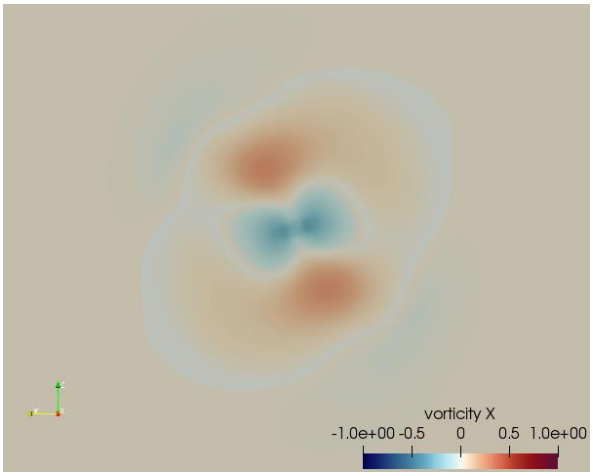

CRP d=0.5D

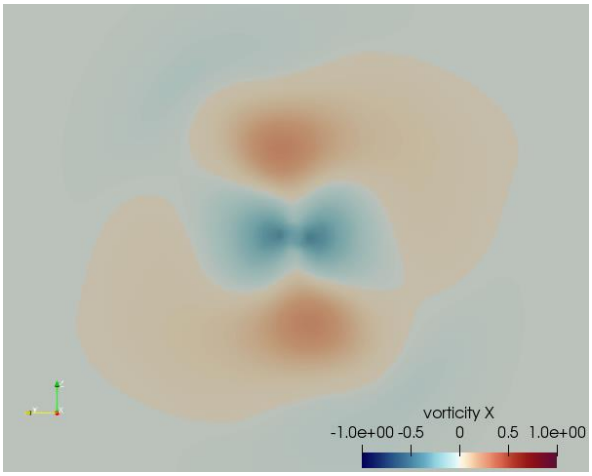

CRP d=1.0D

Figure 4-45: Vorticity field at a downstream distance of 0.25D from the aft propeller for all studied cases

Indeed, the interaction mechanisms are studied only for three spacing with the smaller one being d=0.3D, smaller spacings would have different interaction mechanisms (especially in the pressure field) which could have a significant effect on efficiency. It is also important to note that the individual propellers perform worse than isolated one, but combined they have a similar efficiency. Therefore, more thrust can be produced while preserving the propulsive efficiency making the CRP configuration advantageous in applications where the advance ratio is high enough, and weight is a major concern (as single engine CRPs, weigh less than two isolated propellers).

CONCLUSION

At the end of the present study, the obtained results allowed for a qualitative assessment of an isolated propeller and three contra-rotating propeller configurations with the difference being the inter-propeller distance. Two approaches have been considered: the vortex lattice method (with the OpenVSP software), and the use of computational fluid dynamics with OpenFOAM (RANS with standard k-ε turbulence model) with the sliding mesh technique. Both approaches have been executed in transient mode, since CRPs rotate in different directions and a steady flow approach is simply erroneous in order to capture the interaction between the two propellers. As experimental data for low-Reynolds propellers is available only for commercial ones, the geometry of the propellers is not fully defined for industrial reasons, hence an open-access model was used for the simulations and compared to the closest commercial equivalent. For this reason, the obtained results are intrinsically qualitative.

Several differences between the VLM and CFD approaches have been found, namely in their prediction of the torque coefficient and efficiency. The behaviour of the obtained results lies in a good qualitative agreement with experimental data; and as cases for 3,000 RPM and an upstream velocity of 1m/s are found to be equivalent, the latter are used in CFD. The removal of the hub in VLM can be considered a good hypothesis whereas in CFD, it can be considered as the primary reason for the drop in performance. However, both approaches give performance curves with similar behaviours. Concerning the effects of the inter-propeller distance in CRP configurations, the VLM approach predicts that the spacing has little to no effect on performance for high advance ratios; however the performance difference between the CRP configurations is significant, with performance increasing with spacing (C_T, C_P and η increasing by 24%, 14% and 6.3% respectively).

The increase in performance is best explained by the analysis of the vorticity in the inter-propeller region and the wake of the aft propeller: indeed, the simulations predict that the increase of efficiency with spacing is caused by the conservation of the induced swirl over a longer distance than the turbulent structures which dissipate quite closely to the propeller which generated them.

Based on this work several recommendations can be addressed for future CRP studies, indeed:

- Although removing the hub yields satisfactory results in order to solely asses the inter-propeller distance effects; it would not be advised if the aim of the study is to accurately estimate the performances of a given configuration. However, the meshing process would become more complex and the needed computational resources more extensive;
- The k-ε model is a good first CFD approach that can allow engineers to take design decisions and compare various configurations, but it would be interesting to perform the simulations using a more sophisticated turbulence model for more quantitatively accurate results;
- Unpractical computational times were required for higher quality results with the current workstation, hence high performance computing should be strongly considered if a complete quality description of the CRP systems is needed;
- In future research, wind tunnel tests should be made for a better evaluation of the performances.

BIBLIOGRAPHY

[1] **Árpád Veress, and Rohács József**, "Application of Finite Volume Method in Fluid Dynamics and Inverse Design Based Optimization", In *Finite Volume Method - Powerful Means of Engineering Design*, by Radostina Petrova. InTech (2012).

[2] **Benzamouche Rayane, Bouharaoua Sadjia, and Bentrad Hocine**. *Etude des performances d'une hélice carénée,* University of Saad Dahleb Blida 1 (2023), Master's thesis.

[3] **Bouregba Fatima, and Mustafa Belkadi**. *Optimisation numérique des hélices marines contrarotatives (CRMP),* Université des Sciences et Technologies d'Oran (2021), PhD thesis.

[4] **Brandt John B., and Michael S. Selig**. "Propeller Performance Data at Low Reynolds Numbers", *49th AIAA Aerospace Sciences Meeting.* Orlando: American Institute of Aeronautics and Astronautics (2011).

[5] **Chung, T. J.** *Computational Fluid Dynamics, 2nd Edition,* Cambridge University Press (2010).

[6] **Coleman Colin P.** *A Survey of Theoretical and Experimental Coaxial Rotor Aerodynamic Research,* NASA (1997).

[7] **Colley Eamonn, and Tim Gourlay.** *Analysis of Flow around a Ship Propeller using OpenFOAM.* Perth: Curtin University (2012), Master's thesis.

[8] **Feng Feng, Chong Geng, Ting Guo, Qing-yuan Huang, and Jian Hu.** "Numerical Simulation of Contra Rotating Propellers", *International Conference on Manufacturing Engineering and Intelligent Materials (ICMEIM 2017).* Atlantis Press (2017), 543-548.

[9] **Grassi Davide, Stefano Brizzolara, Michele Viviani, Luca Savio, and Sara Caviglia**, "Design and analysis of counter-rotating propellers-comparison of numerical and experimental results", *Journal of Hydrodynamics* (2010), 553-559, DOI: 10.1016/S1001-6058(09)60254-7.

[10] **Kravitz Eyal, Chryssostomos Chryssostomidis**. *Analysis and Experiments for Contra-Rotating Propeller,* Massachusetts Institute of Technology (2011), Master's thesis.

[11] **Launder B. E., and Spalding D. P.**, "The Numerical Computation of Turbulent Flows", *Computer Methods in Applied Mechanics and Engineering*, (1974), 269-289.

[12] **Lopez Jorge, and Aitor Juando**. "Development of Standardized Series of Counter-Rotating Propellers with Special Interest in Hydrofoil Navigation", *25th Numerical Towing Tank Symposium (NuTTS).* Ericeira, Portugal (2023).

[13] **McCoy H. M.**, "Counter-Rotating Propellers", *Eight Annual Meeting of the Institute of the Aeronautical Sciences.* New York City (1940).

[14] **McDonald Robert A. and James R. Gloudemans**, "Open Vehicle Sketch Pad: An Open Source Parametric Geometry and Analysis Tool for Conceptual Aircraft Design", *AIAA SciTech 2022 Forum.* San Diego: American Institute of Aeronautics and Astronautics, DOI: 10.2514/6.2022-0004 (2022).

[15] **Panjwani Balram, Quinsard Cecile, Gacia Dominik, Przemysław and Jostein Furseth**, "Virtual Modeling and Testing of the Single and Contra-Rotating Co-Axial Propeller", *Drones, Vol. 4, No. 3* (2020), DOI:10.3390/drones4030042.

[16] **Rhee Shin Hyung and Shitalkumar Joshi**. "Computational Validation for Flow around a Marine Propeller Using Unstructured Mesh Based Navier-Stokes Solver", *JSME International Journal Series B, Vol. 48, No. 3* (2005), 562-570, DOI: 10.1299/jsmeb.48.562.

[17] **Russo Nicola, Aniello Daniele Marano, Giuseppe Maurizio Gagliardi, Michele Guida, Tiziano Pollito, and Francesco Marulo**, "Thrust and Noise Experimental Assessment on Counter-Rotating Coaxial Rotors", *Aerospace, Vol. 10, No. 6* (2023), DOI: 10.3390/aerospace10060535

[18] **Sercan Özturk, and Aksel M. Haluk**, *Design and Performance Analysis of Counter Rotating Propeller.* Middle East Technical University (2022), Master's thesis.

[19] **Spakovsky Z. S.**, *Production of Thrust with a Propeller* (2009). https://web.mit.edu/16.unified/www/SPRING/propulsion/UnifiedPropulsion7/UnifiedPropulsion7.htm (accessed 2024).

[20] **Stajuda Mateusz, Maciej Karczewski, Damian Obidowski, and Krzysztof Jozvik**, "Development of a CFD model for propeller simulation", *Mechanics and Mechanical Engineering, Vol. 20, No. 4* (2016), 579-593.

[21] **Štorch Vít**, *Verified Unsteady Model for Analysis of Contra-Rotating Propeller Aerodynamics.* Prague: Czech Technical University in Prague (2017), PhD thesis.

[22] **Su Shichuan, Shengsen Wang, Jiabin Cao, and Desheng Feng**,"Prediction of hydrodynamic characteristics of combined propellers based on CFD method", *3rd International Conference on Fluid Mechanics and Industrial Applications.* Journal of Physics, C. Series (2019), DOI: 10.1088/1742-6596/1300/1/012016.

[23] **The OpenFOAM Foundation**, https://openfoam.org/ (accessed 2024).

[24] **Thiele Moritz, Martin Obster, and Miriko Hornung**,"Aerodynamic Modeling of Coaxial Counter-Rotating UAV Propellers", *8th Biennial Autonomous VTOL Technical Meeting.* Mesa, Arizona, USA: The Vertical Flight Society (2019).

[25] **Triet Pham Minh, Phan Quoc Thien, and Ngo Khanh Hieu**,"CFD simulation for the Wageningen B-Series propeller characteristics in open-water condition using k-epsilon turbulence model", *Science and Technology Development Journal, Vol. 1, No. 1* (2018), 35-42.

[26] **Weick Fred E.**, *Aircraft Propeller Design, B. S.* McGraw-Hill Book Company (1930).

[27] **Wenhui Yan and Zhang Kun**, "Effects of Stage Spacing on Contra-Rotating Propeller Aerodynamic Interactions", *2022 International Conference on Defence Technology (2022 ICDT).* Journal of Physics: Conf. Series (2023), DOI: 10.1088/1742-6596/2478/12/122013.